Supplementary Information for

Diethoxycarbonyl-BODIPYs as heavy-atom-free photosensitizers for holographic recording in cellulose acetate photopolymer

Aimee Sheehan, Tatsiana Mikulchyk, Catherine S. P. De Castro, Safakath Karuthedath, Wejdan Althobaiti, Metodej Dvoracek, Sabad-e- Gul, Hugh J. Byrne, Frédéric Laquai, Izabela Naydenova and Mikhail A. Filatov*

E-mail: *mikhail.filatov@tudublin.ie*

Table of Contents

1. General procedures

UV-Vis absorption spectra were recorded in solutions using Shimadzu UV-1900i, Cary 5000 and PerkinElmer Lambda 900 UV/VIS/NIR spectrometers (1 cm path length quartz cell). Fluorescence emission spectra were measured using FluoroMax-4 and PerkinElmer LS 55 luminescence spectrometers. Emission quantum yields of the compounds were measured relative to the fluorescence of Rhodamine 6G in ethanol (Φ_{em} = 0.95).[1] Sample concentrations were chosen to obtain an absorbance of 0.03-0.07 at the excitation wavelength; at least three measurements were performed for each sample.

NMR spectra were recorded on a Bruker Avance II 400 MHz or a Bruker Avance III 500 MHz spectrometer. Accurate mass measurements (HRMS) were performed in the UCD School of Chemistry Mass Spectrometry Facility. Samples were run on an Agilent 6546 QToF (Quadrupole Time-of-Flight Mass Spectrometer) with an Agilent 1260 Infinity Prime II quaternary pump; chromatography was effected via a 50mm Agilent Poroshell 2.7um C18 column. LC Mobile phases and buffers were A: H2O with 0.1% Formic Acid. B: ACN with 0.1% Formic Acid. Gradient was: 90% A / 10% B (time 0 min); 10% A / 90% B (time 5 min); 10% A / 90% B (time 10 min). Data analysis was carried out using Agilent Masshunter software.

Melting points were measured using an automated melting point meter SMP10 (Stuart) and are uncorrected.

2. Dyes synthesis and characterization

The handling of all air/water sensitive materials was carried out using standard high vacuum techniques. Tetrahydrofuran and dichloromethane were distilled from $LiAlH_4$ and CaH_2, respectively. All other solvents were used as commercially supplied. Analytical thin layer chromatography was performed using silica gel 60 (fluorescence indicator F254, pre-coated sheets, 0.2 mm thick, 20 cm × 20 cm; Merck) plates and visualized by UV irradiation (λ = 254 nm). Column chromatography was carried out using Fluka Silica Gel 60 (230–400 mesh).

10-Methylanthracene-9-carbaldehyde, 9-anthracenecarboxaldehyde, pyrene-1-carbaldehyde, benzaldehyde, *p*-anisaldehyde, 2,5-dimethoxybenzaldehyde, 2,4,6-trimethoxybenzaldehyyde, dimethoxymethane, 2,3-dichloro-5,6-dicyano-1,4-benzoquinone, boron trifluoride diethyl etherate and N,N-diisopropylethylamine were purchased from Sigma-Aldrich. Ethyl 2,4-dimethyl-1H-pyrrole-3-carboxylate was prepared according to the reported procedure.[2]

Synthesis of BODIPY 1

A mixture of ethyl 2,4-dimethyl-1H-pyrrole-3-carboxylate (1 g, 5.99 mmol), dimethoxymethane (0.533 g, 7 mmol), and p-toluenesulfonic acid monohydrate (0.05 g, 0.263 mmol) was dissolved in acetic acid (50 mL) and stirred at room temperature under inert atmosphere for 18 h. The resulting mixture was poured into cold water (100 mL). The precipitate formed was filtered on vacuum, washed with 50 mL of water and dried on air for 12 h. Obtained solid material was then mixed with anhydrous dichloromethane (50 mL) and 2,3-dichloro-5,6-dicyano-1,4-benzoquinone (DDQ) (0.681 g, 3 mmol) was added. The reaction mixture turned black and stirring was continued for another 20 min. The reaction mixture was then transferred into a separating funnel and washed with water (2 × 50 mL). Organic phase was separated, dried over Na_2SO_4 and evaporated to dryness in vacuum. The solid residue was re-dissolved in anhydrous dichloromethane (50 mL) and N-ethyl-diisopropylamine (3.48 mL, 20 mmol) and BF_3•Et_2O (2.46 mL, 20 mmol) were added under stirring. The reaction mixture was stirred for 1 h under inert atmosphere. The reaction mixture was transferred into a separation funnel and washed with water (2 × 50 mL). The organic phases were combined, dried over Na_2SO_4 and evaporated to dryness in vacuum. The crude product was purified by silica gel column chromatography (eluent - dichloromethane).

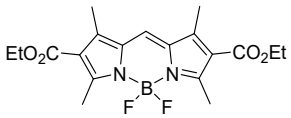

Compound **1**. Orange crystalline solid, m.p. 267 °C, 29 % yield. ^{1}H NMR (400 MHz, $CDCl_3$) δ 7.40 (s, 1H), 4.33 (q, *J* = 7.2 Hz, 4H), 2.83 (s, 6H), 2.53 (s, 6H), 1.39 (s, 6H). ^{13}C NMR (100 MHz, $CDCl_3$) δ 164.23, 161.30, 146.04, 133.12, 123.47, 121.05, 60.40, 15.20, 14.52, 12.21. HRMS (ESI): *m/z* found 393.1793, calcd for $(M+H)^+$ $C_{19}H_{24}BF_2N_2O_4$ 393.1797.

General procedure for the synthesis of BODIPYs 1a-g

Ethyl 2,4-dimethyl-1H-pyrrole-3-carboxylate (3 mmol) and corresponding aldehyde (1.5 mmol) were dissolved in anhydrous dichloromethane (30 mL) and the solution was degassed by bubbling nitrogen for 10 min. Trifluoroacetic acid (30 μL, 0.392 mmol) was added and the reaction mixture was stirred for 12 h under inert atmosphere. 2,3-Dichloro-5,6-dicyano-1,4-benzoquinone (DDQ) (0.3405 g, 1.5 mmol) was added and the mixture was stirred for another 20 min. The reaction mixture was then transferred into a separating funnel and washed with water (2 × 30 mL). The organic phase was separated, dried over Na_2SO_4 and evaporated to dryness in vacuum. The solid residue was re-dissolved in anhydrous dichloromethane (30 mL) and N-ethyl-diisopropylamine (0.87 mL, 5 mmol) and BF_3•Et_2O (0.62 mL, 5 mmol) were added under stirring. The reaction mixture was stirred for 1 h under inert atmosphere. The reaction mixture was

transferred into a separation funnel and washed with water (2 × 30 mL). The organic phases were combined, dried over Na_2SO_4 and evaporated to dryness in vacuum. The crude products were purified by silica gel column chromatography (eluent - dichloromethane) to afford analytically pure compounds.

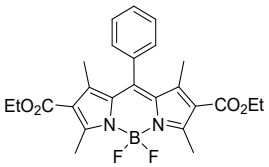

Compound **1a**. Orange crystalline solid, m.p. 199 °C, 9 % yield. ^{1}H NMR (500 MHz, $CDCl_3$) δ 7.56 – 7.52 (m, 3H), 7.29 – 7.26 (m, 2H), 4.28 (q, J = 7.1 Hz, 4H), 2.83 (s, 6H), 1.65 (s, 6H), 1.32 (t, J = 7.1 Hz, 6H). ^{13}C NMR (126 MHz, $CDCl_3$) δ 164.44, 159.64, 147.83, 145.97, 134.55, 131.59, 129.85, 129.77, 129.12, 128.55, 127.88, 122.68, 60.38, 15.14, 14.43, 13.78. HRMS (ESI): *m/z* found 469.2110, calcd for $(M+H)^+$ $C_{25}H_{28}BF_2N_2O_4$ 469.2110.

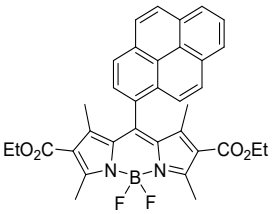

Compound **1b**. Orange crystalline solid, m.p. 260 °C, 34 % yield. ^{1}H NMR (400 MHz, $CDCl_3$) δ 8.33 (d, *J* = 7.9 Hz, 1H), 8.29 (d, *J* = 7.6 Hz, 1H), 8.25 – 8.15 (m, 3H), 8.09 (dd, *J* = 8.3, 7.2 Hz, 2H), 7.92 (d, *J* = 9.1 Hz, 1H), 7.85 (d, *J* = 7.8 Hz, 1H), 4.20 (q, *J* = 7.1 Hz, 4H), 2.90 (s, 6H), 1.24 (t, *J* = 7.1 Hz, 6H), 1.18 (s, 6H). ^{13}C NMR (100 MHz, $CDCl_3$) δ 164.37, 159.86, 147.76, 145.15, 132.33, 131.41, 131.08, 129.65, 129.34, 128.95, 128.56, 127.38, 126.86, 126.29, 126.15, 125.80, 125.48, 124.89, 124.58, 123.63, 122.76, 122.73, 60.35, 15.23, 14.35, 13.20. HRMS (ESI): *m/z* found 593.2423, calcd for $(M+H)^+$ $C_{35}H_{32}BF_2N_2O_4$ 593.2423.

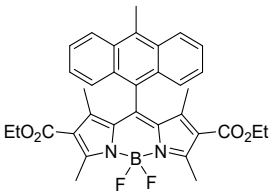

Compound **1c**. Red crystalline solid, m.p. 240 °C, 39 % yield. ^{1}H NMR (400 MHz, $CDCl_3$) δ 8.37 (d, *J* = 8.9 Hz, 2H), 7.80 (d, *J* = 8.5 Hz, 2H), 7.55 (ddd, *J* = 8.9, 6.5, 1.2 Hz, 2H), 7.43 (ddd, *J* = 8.6, 6.5, 1.1 Hz, 2H), 4.18 (q, *J* = 7.1 Hz, 4H), 3.22 (s, *3*H), 2.91 (s, 3H), 1.23 (t, *J* = 7.1 Hz, 6H), 0.96 (s, 6H). ^{13}C NMR (100 MHz, $CDCl_3$) δ 164.36, 159.79, 147.48, 144.66, 133.60, 132.62, 130.08, 129.28, 127.06, 125.98, 125.40, 125.20, 122.54, 60.31, 15.24, 14.69, 14.35, 12.56. HRMS (ESI): *m/z* found 583.2582, calcd for $(M+H)^+$ $C_{34}H_{34}BF_2N_2O_4$ 583.2580.

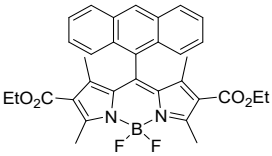

Compound **1d**. Red crystalline solid, m.p. 256 °C, 17 % yield. ^{1}H NMR (500 MHz, $CDCl_3$) δ 8.63 (s, 1H), 8.06 (d, *J* = 8.5 Hz, 2H), 7.79 (dd, *J* = 8.7, 0.8 Hz, 2H), 7.54 – 7.49 (m, 2H), 7.47 – 7.42 (m, 2H), 4.18 (q, *J* = 7.1 Hz, 4H), 2.91 (s, 6H), 1.23 (t, *J* = 7.1 Hz, 6H), 0.96 (s, 6H). ^{13}C NMR (126 MHz, $CDCl_3$) δ 164.50, 160.14, 147.59, 144.07, 132.62, 131.70, 129.83, 129.41, 128.92, 127.85, 126.34, 124.86, 60.51, 15.44, 14.53, 12.65. HRMS (ESI): *m/z* found 569.2426, calcd for $(M+H)^+$ $C_{33}H_{31}BF_2N_2O_4$ 569.2423.

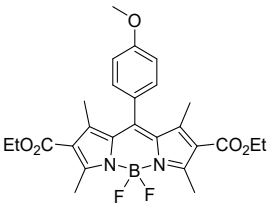

Compound **1e**. Orange crystalline solid, m.p. 204 °C, 28 % yield. ^{1}H NMR (400 MHz, $CDCl_3$) δ 7.20 – 7.11 (m, 2H), 7.09 – 6.94 (m , 2H), 4.28 (q, *J* = 7.1 Hz, 4H), 3.89 (s, 3H), 2.83 (s, 6H), 1.71 (s, 6H), 1.33 (t, *J* = 7.1 Hz, 6H).^{13}C NMR (101 MHz, CDCl3) δ 164.35, 160.74, 159.31, 147.71, 146.07, 131.87, 129.09, 126.32, 122.44, 115.06, 60.22, 55.40, 14.97, 14.29, 13.89. HRMS (ESI): *m/z* found 499.2213, calcd for $(M+H)^+$ $C_{26}H_{30}BF_2N_2O_5$ 499.2216.

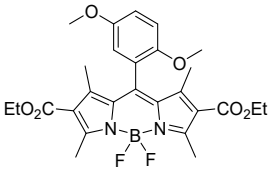

Compound **1f**. Orange crystalline solid, m.p. 177 °C, 20 % yield. ^{1}H NMR (500 MHz, CDCl3) δ 7.02 (dd, J = 9.0, 3.1 Hz, 1H), 6.94 (d, J = 9.1 Hz, 1H), 6.68 (d, J = 3.0 Hz, 1H), 4.28 (q, J = 7.1 Hz, 4H), 3.77 (s, 3H), 3.73 (s, 3H), 2.83 (s, 6H), 1.79 (s, 6H), 1.33 (t, J = 7.1 Hz, 6H). ^{13}C NMR (126 MHz, $CDCl_3$) δ 164.55, 159.25, 155.04, 150.26, 147.37, 131.63, 123.88, 116.46, 114.54, 112.76, 60.32, 56.24, 56.10, 15.18, 14.46, 13.01. HRMS (ESI): *m/z* found 529.2324, calcd for $(M+H)^+$ $C_{27}H_{32}BF_2N_2O_6$ 529.2321.

Compound **1g**. Orange crystalline solid, m.p. 185 °C, 17 % yield. ^{1}H NMR (500 MHz, $CDCl_3$) δ 6.23 (s, 2H), 4.28 (q, *J* = 7.1 Hz, 4H), 3.88 (d, *J* = 4.2 Hz, 3H), 3.70 (s, 6H), 2.82 (s, 6H), 1.88 (s, 6H), 1.33 (t, *J* = 7.1 Hz, 6H). ^{13}C NMR (126 MHz, $CDCl_3$) δ 164.76, 163.29, 158.41, 157.85, 146.85, 141.11, 132.34, 121.80, 104.54, 91.27, 70.92, 60.19, 56.10, 55.61, 15.14, 14.46, 12.52. HRMS (ESI): *m/z* found 559.2428, calcd for M^+ $C_{28}H_{34}BF_2N_2O_7$ 559.2427.

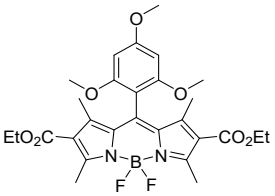

3. NMR spectra

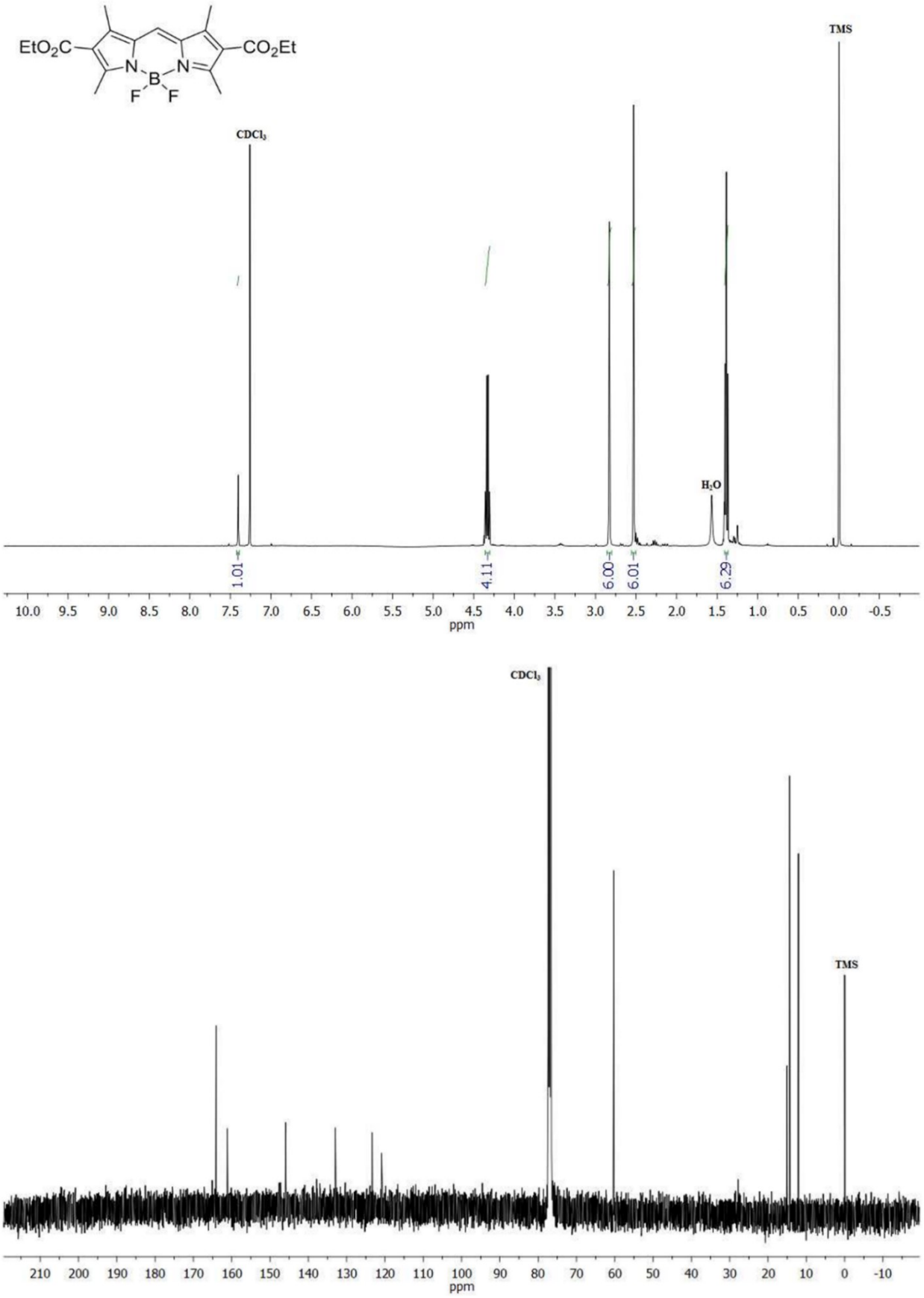

Figure S1. ^{1}H and ^{13}C NMR spectra of compound **1**.

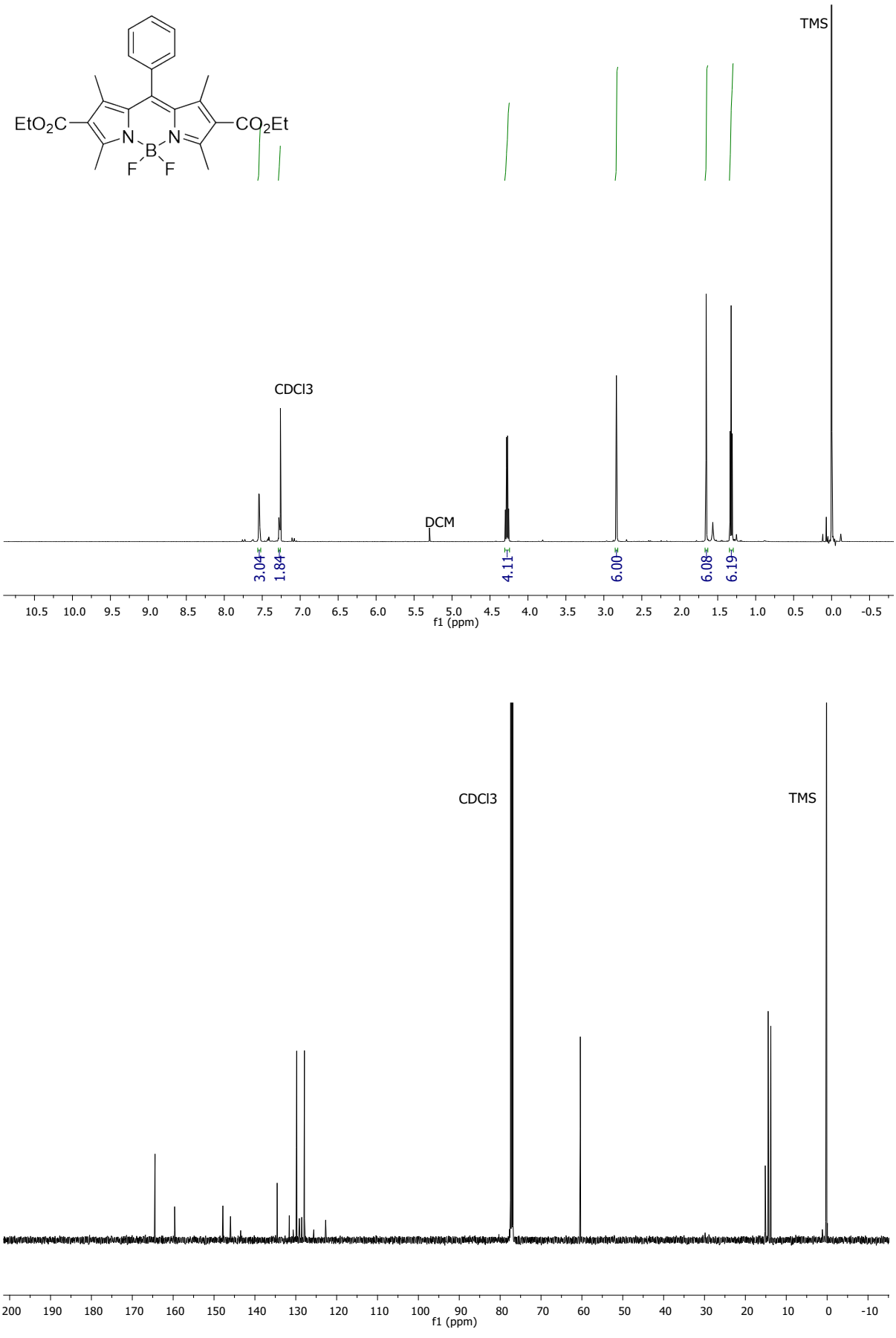

Figure S2. ^{1}H and ^{13}C NMR spectra of compound **1a**.

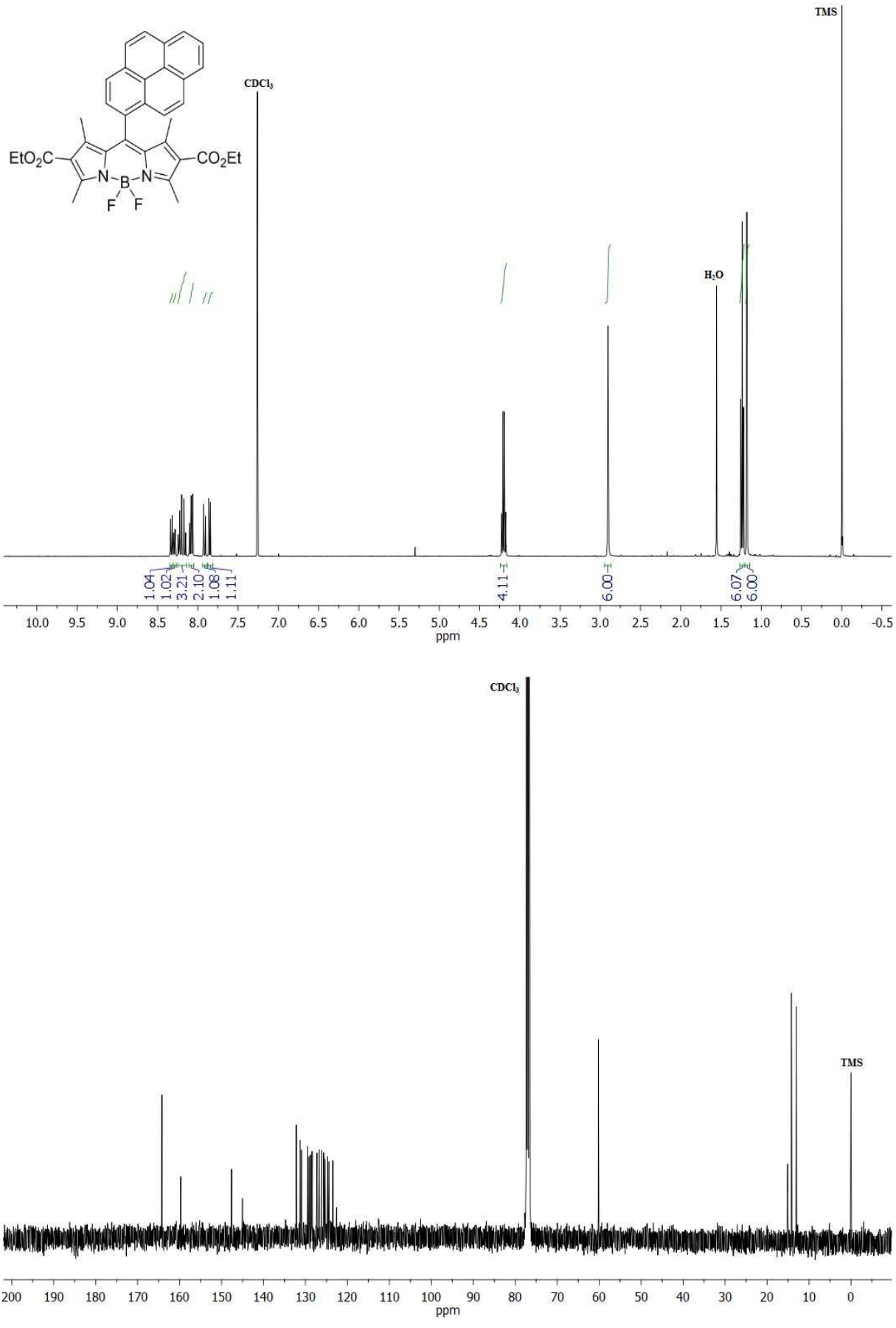

Figure S3. ^{1}H and ^{13}C NMR spectra of compound **1b**.

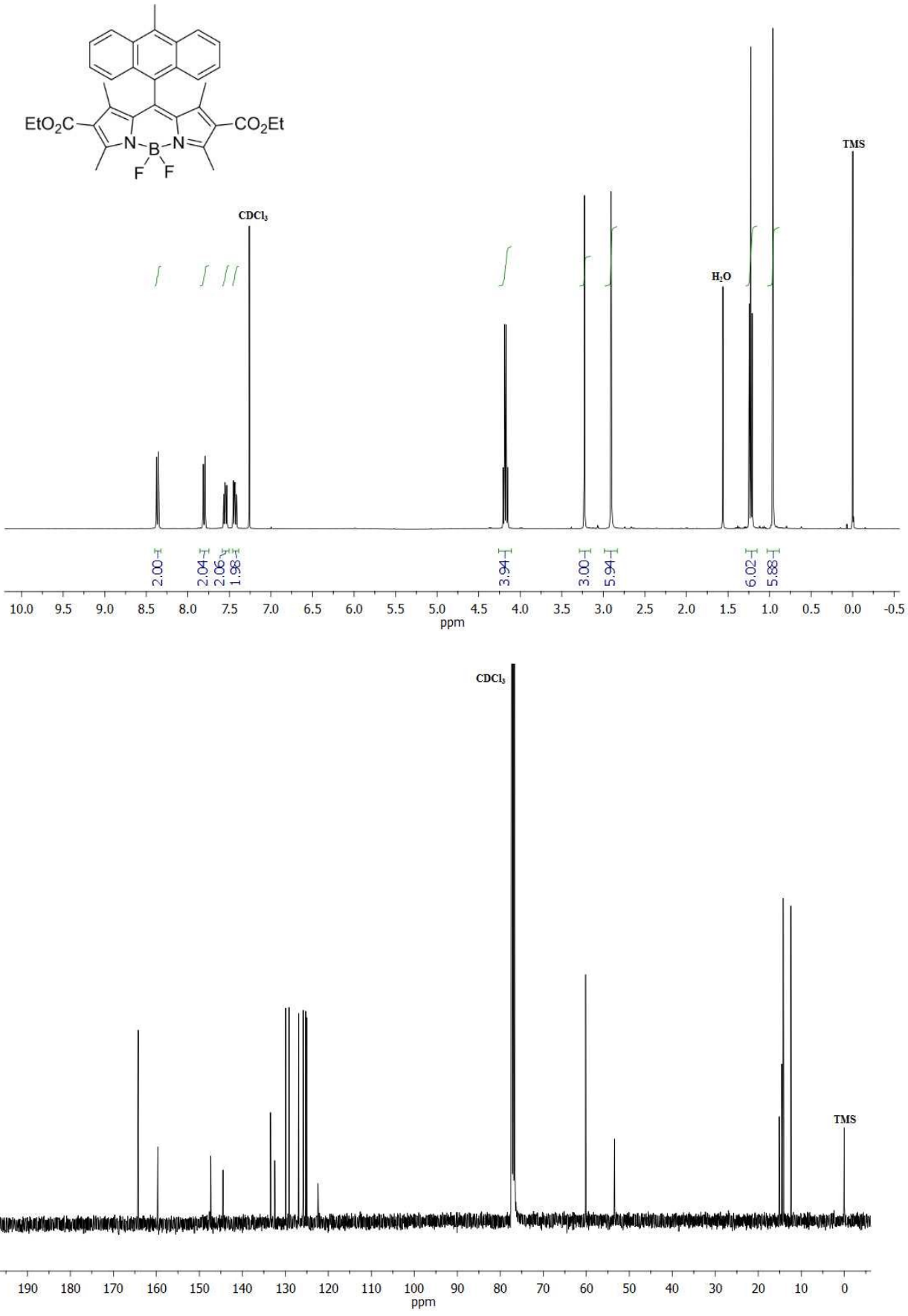

Figure S4. ^{1}H and ^{13}C NMR spectra of compound **1c**.

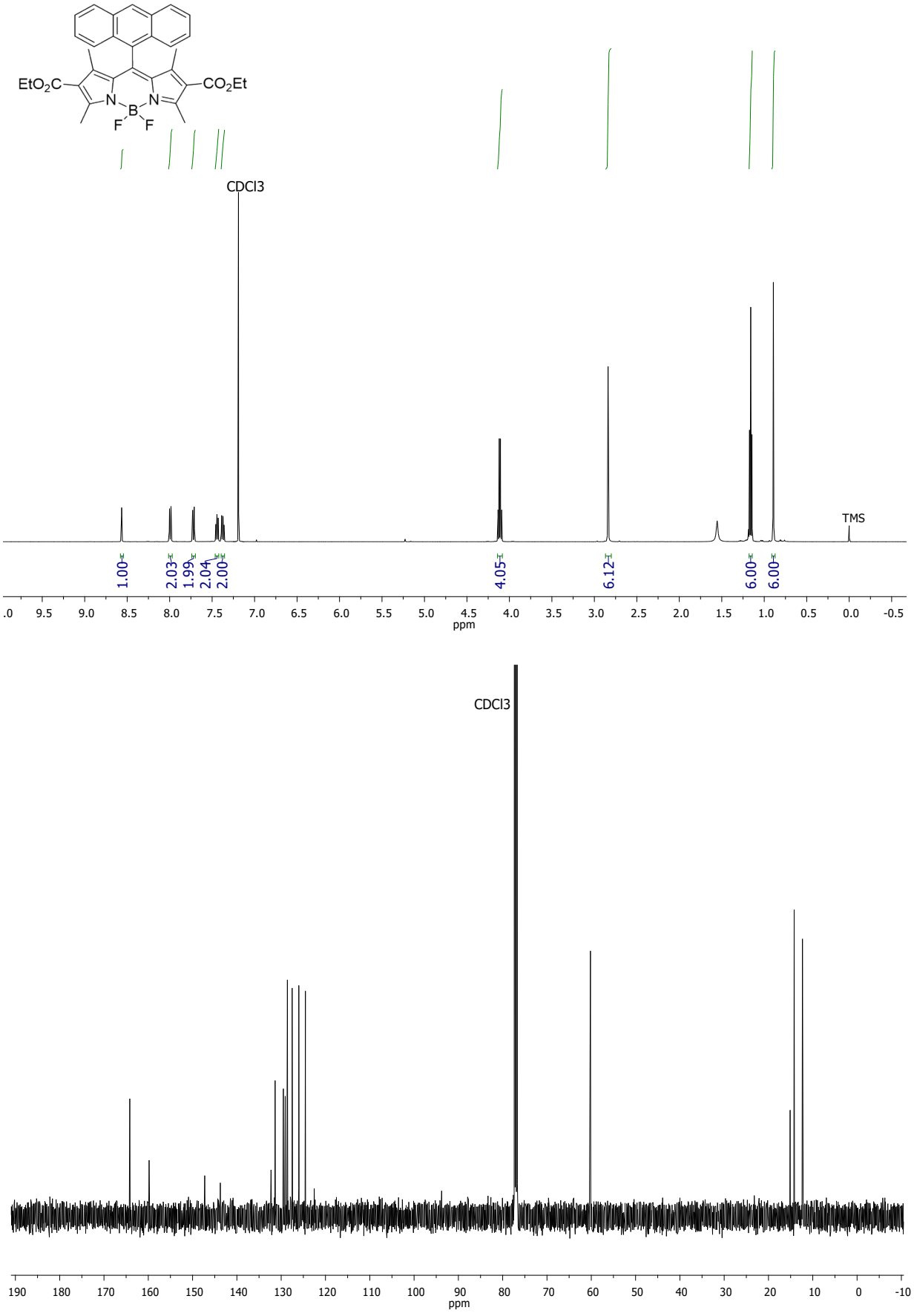

Figure S5. ^{1}H and ^{13}C NMR spectra of compound **1d**.

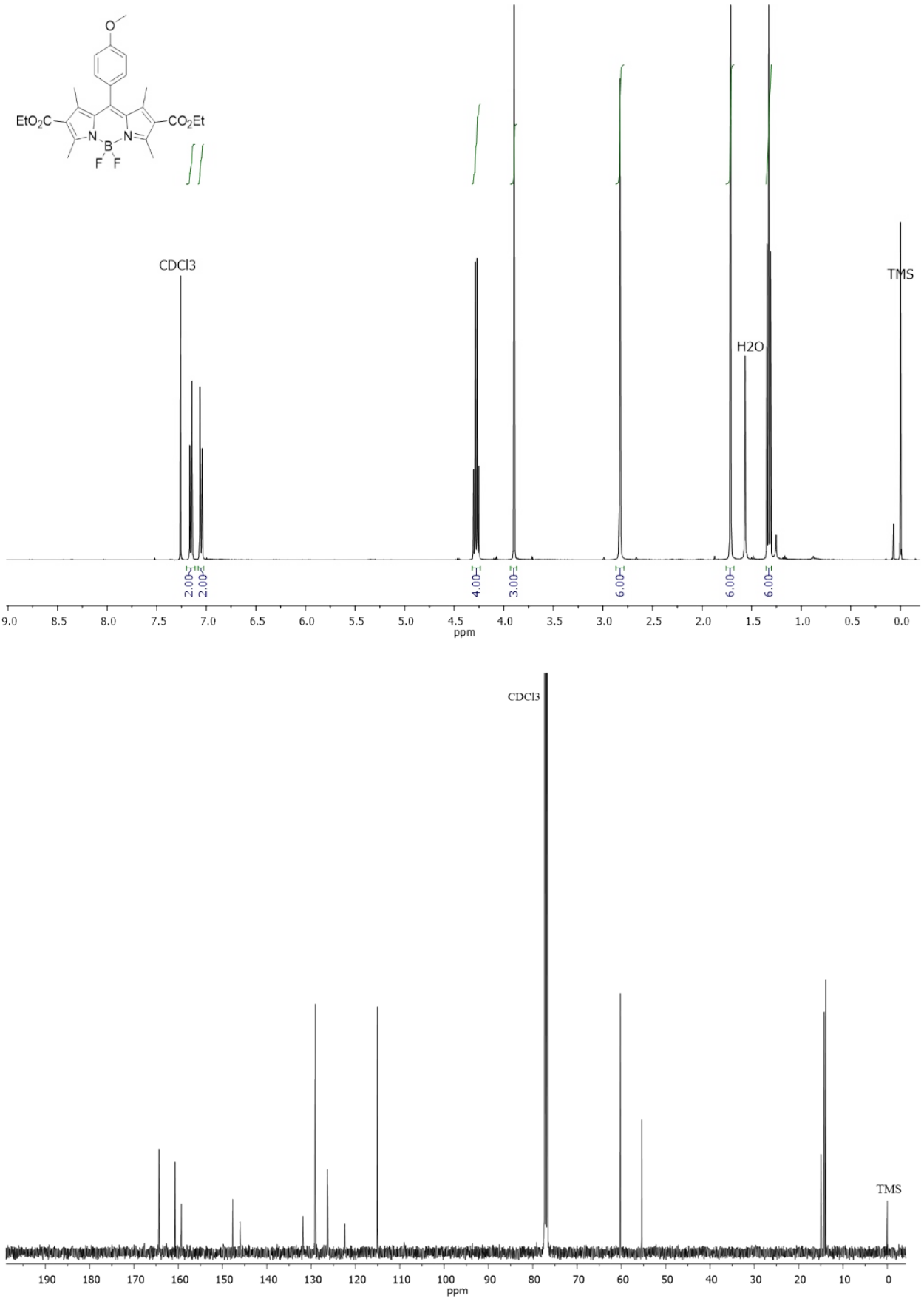

Figure S6. ^{1}H and ^{13}C NMR spectra of compound **1e**.

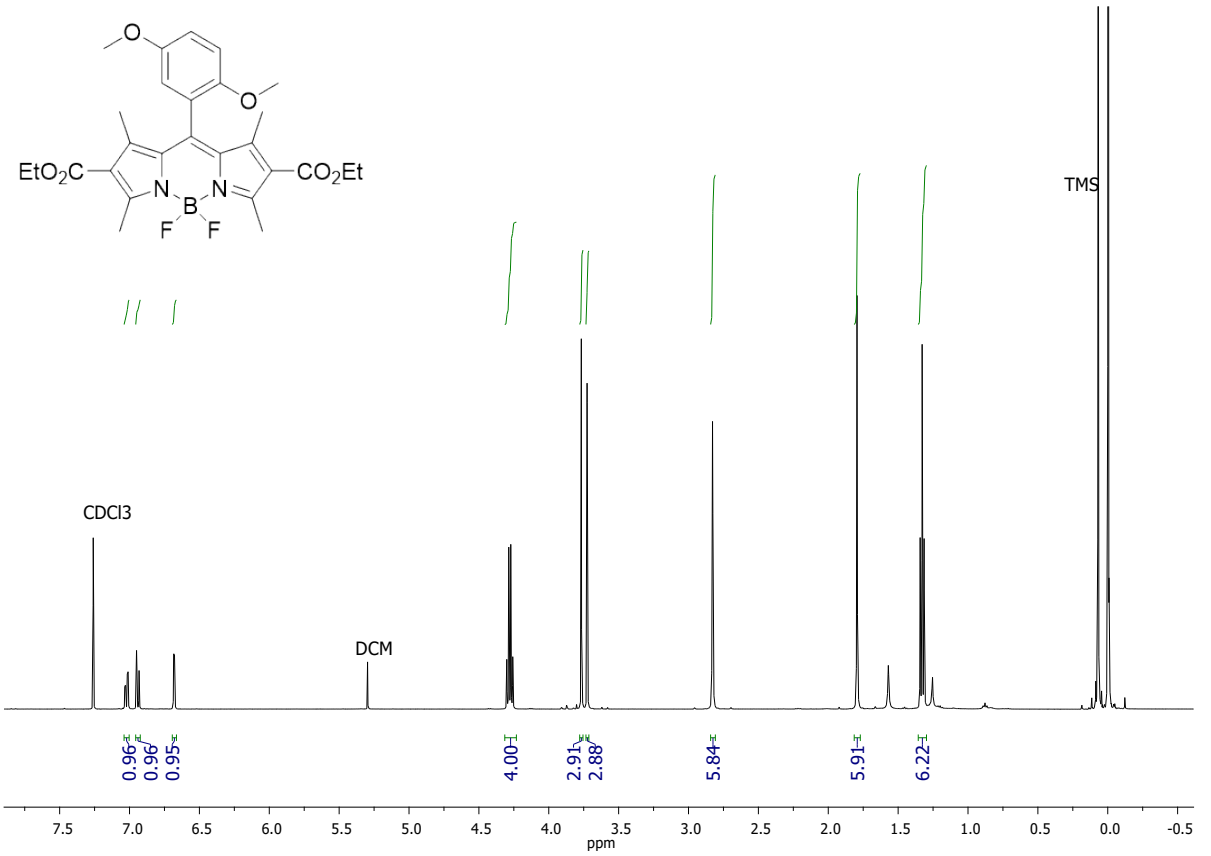
EtO2C
CO2Et
N
B
N
F
F
O
O
CDCl3
DCM
TMS
0.96
0.96
0.95
4.00
2.91
2.88
5.84
5.91
6.22
7.5
7.0
6.5
6.0
5.5
5.0
4.5
4.0
3.5
3.0
2.5
2.0
1.5
1.0
0.5
0.0
-0.5
ppm

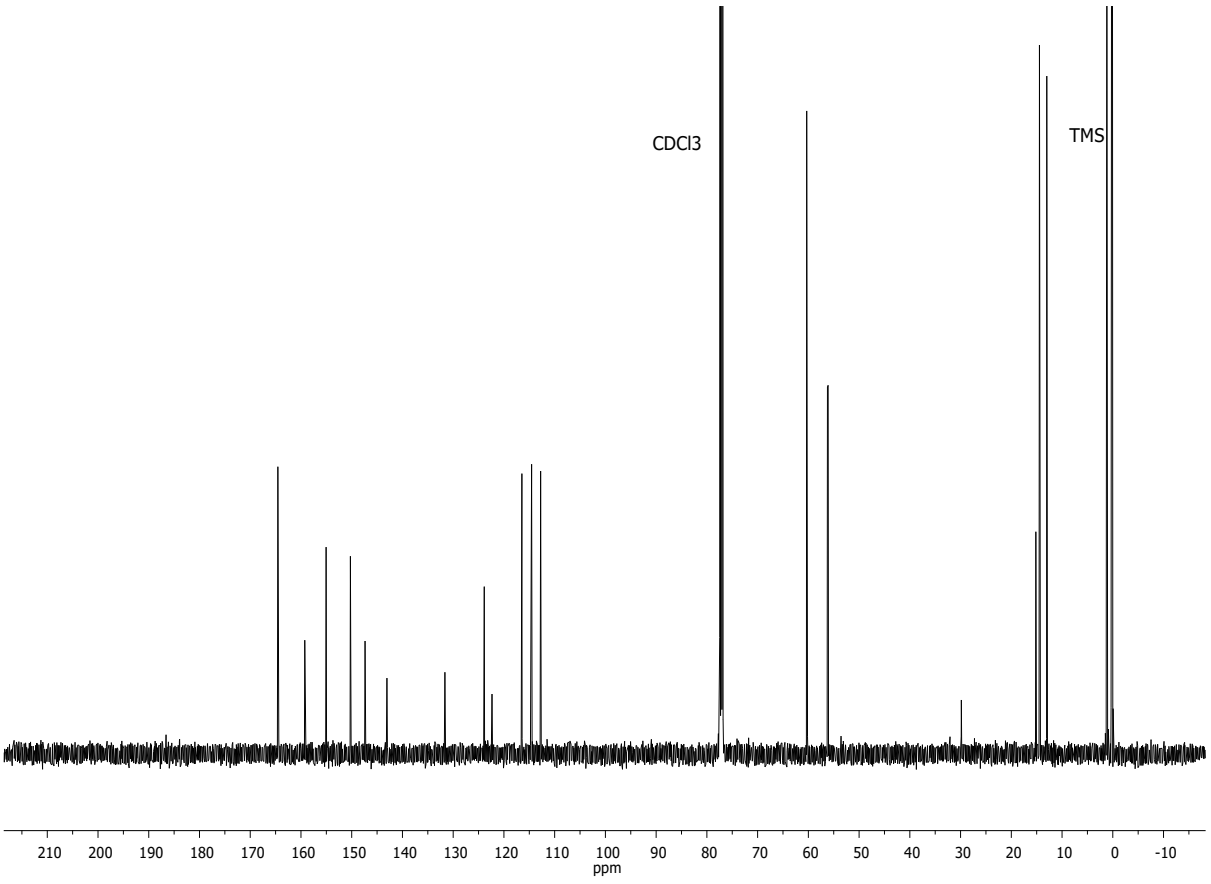
CDCl3
TMS
210
200
190
180
170
160
150
140
130
120
110
100
90
80
70
60
50
40
30
20
10
0
-10
ppm

Figure S7. ^{1}H and ^{13}C NMR spectra of compound **1f**.

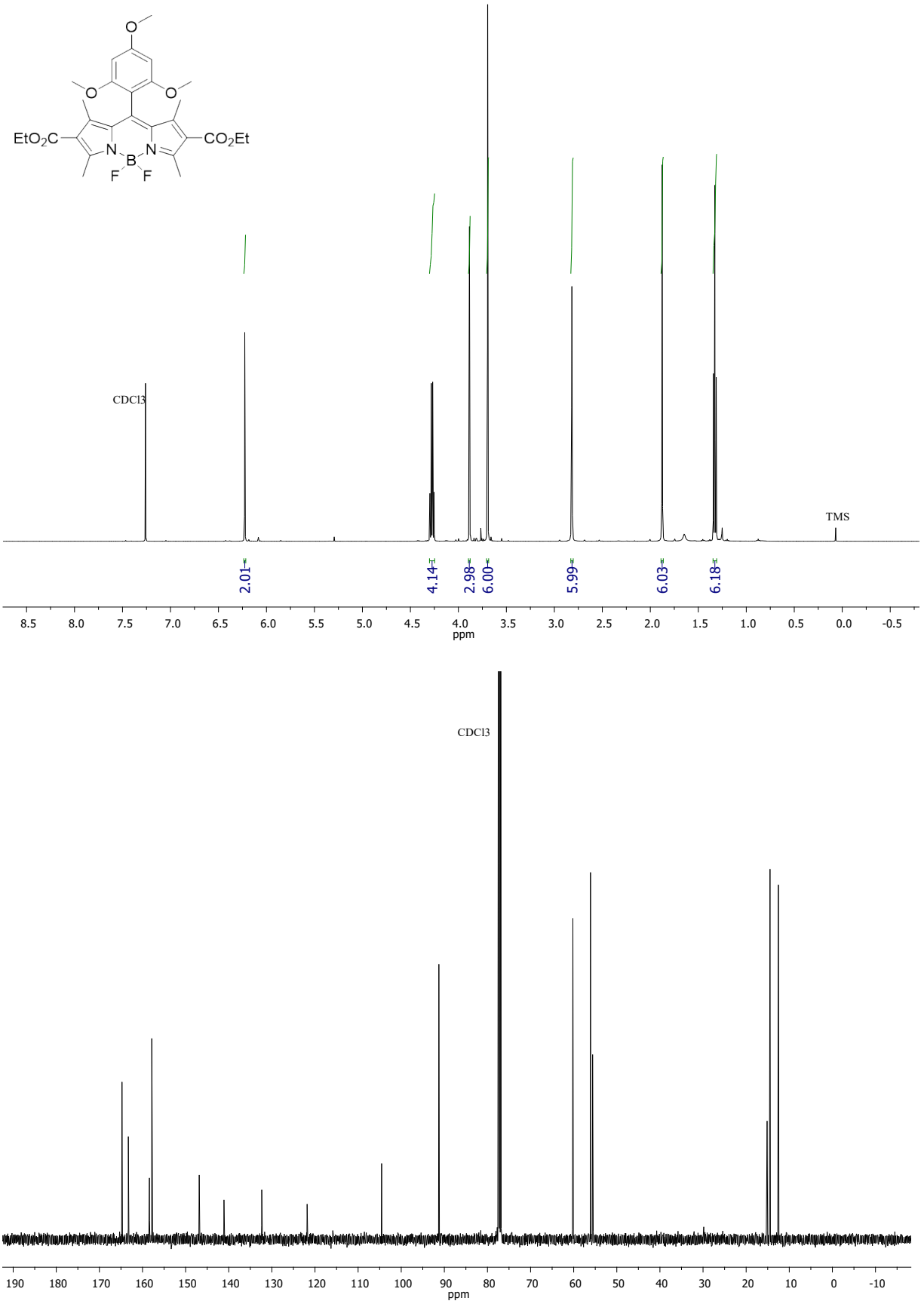

Figure S8. ^{1}H and ^{13}C NMR spectra of compound **1g**.

4. Mass spectra

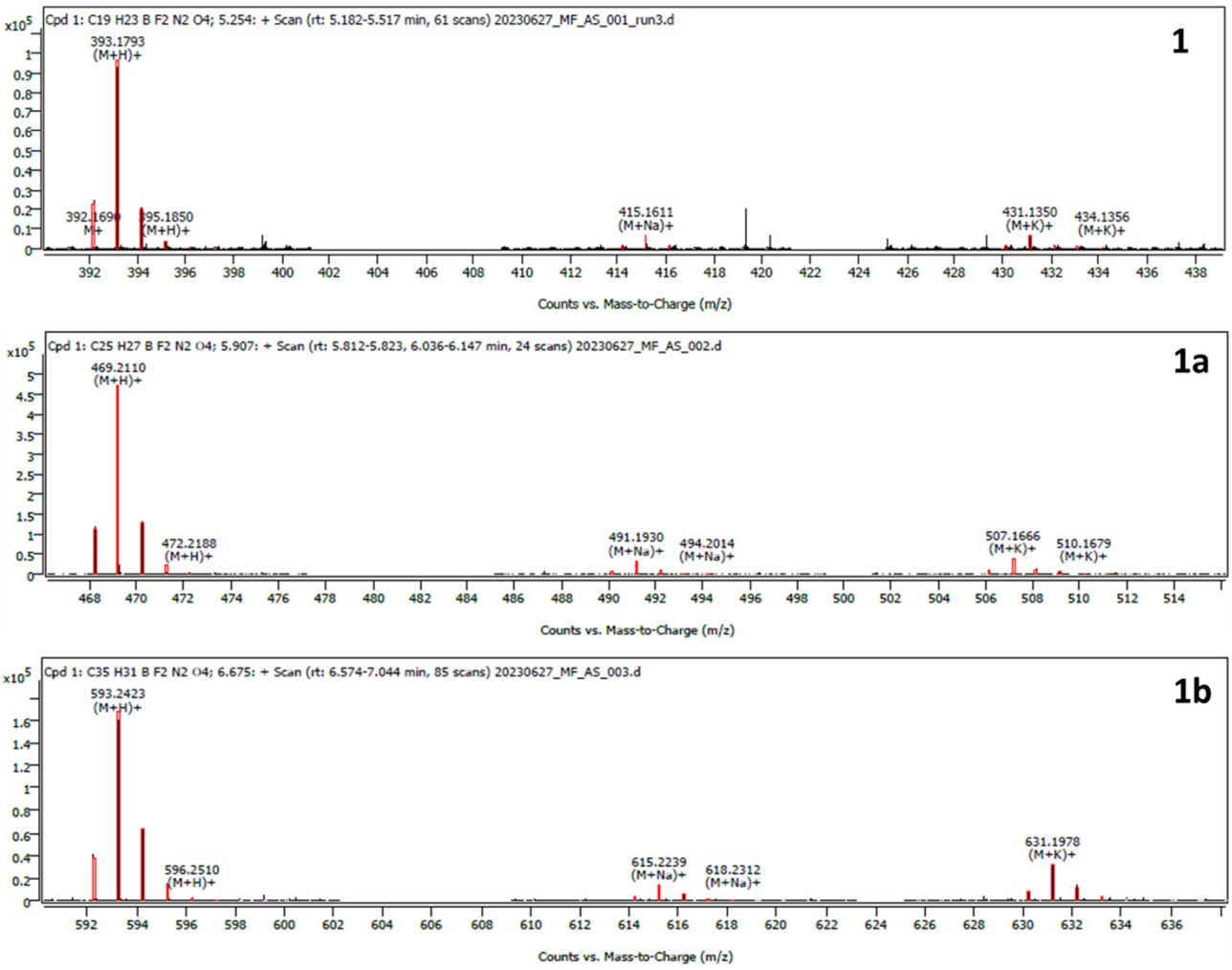

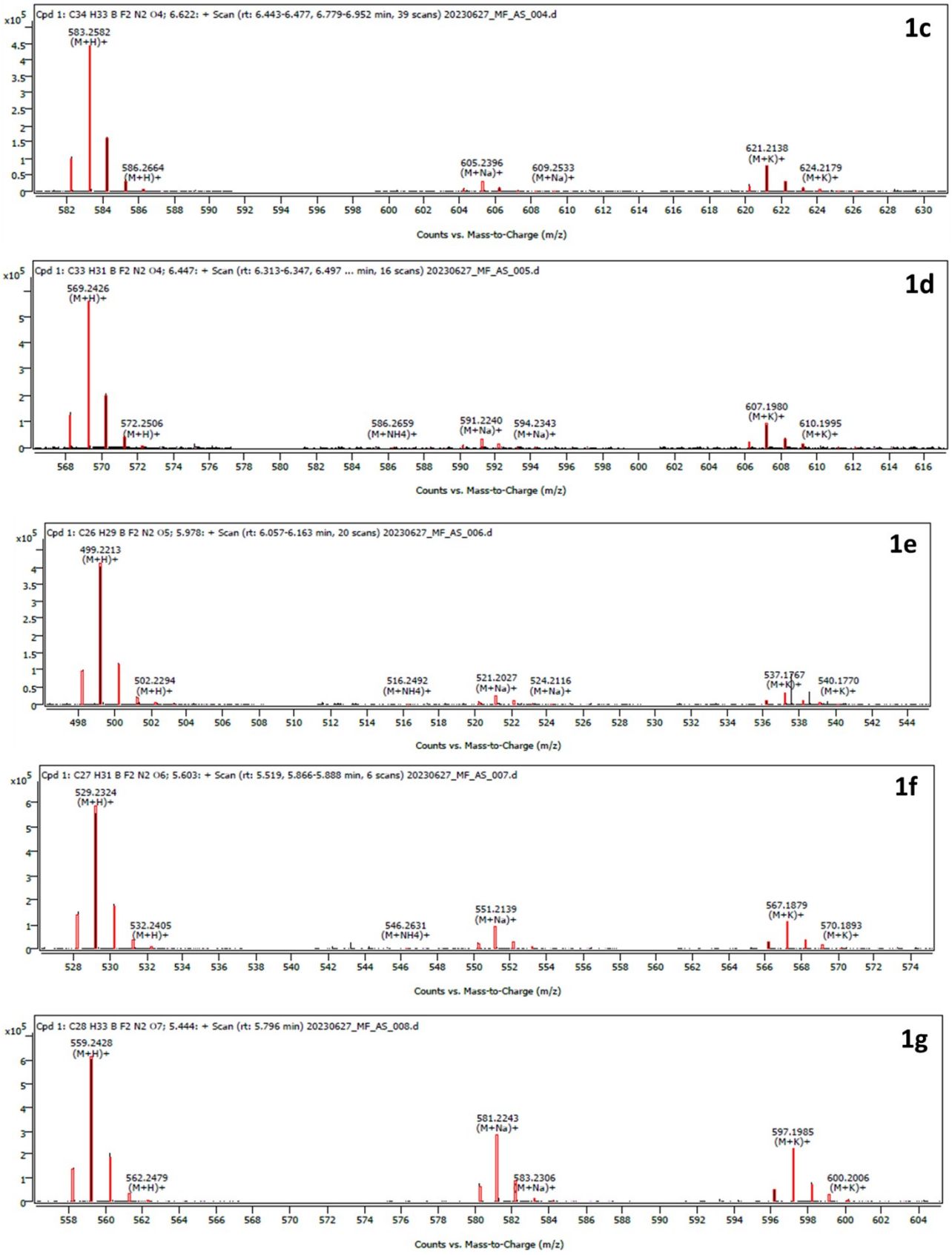

Figure S9. QTOF HRMS spectra of compounds **1a-g** (positive mode).

5. UV-Vis absorption and photoluminescence spectra

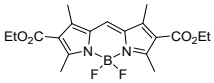

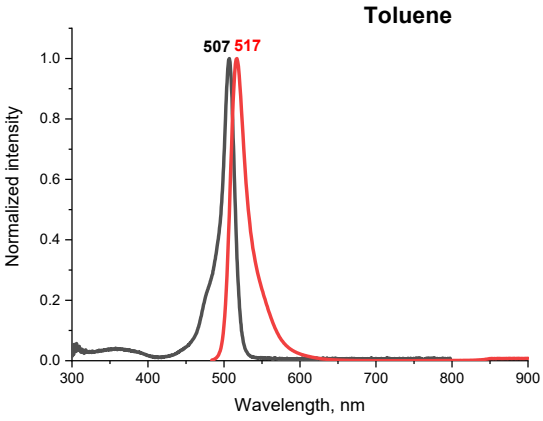

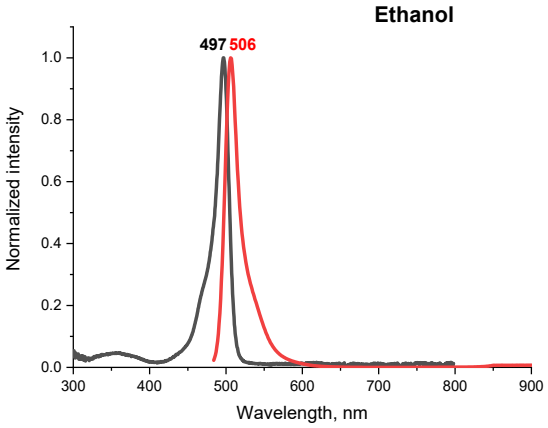

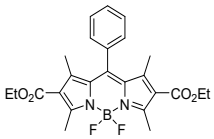

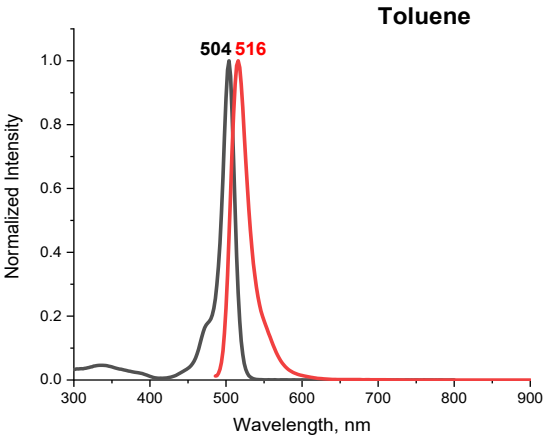

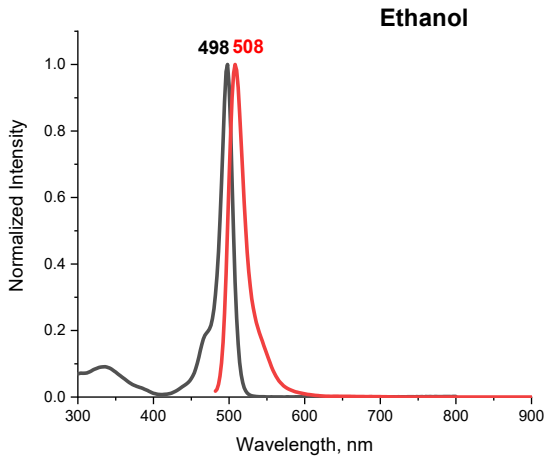

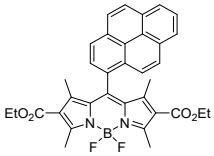

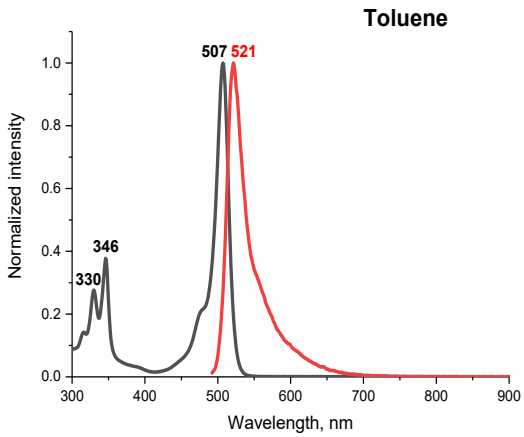

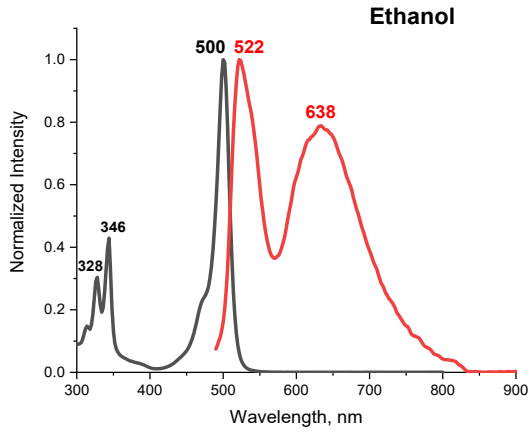

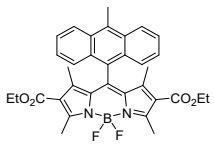
EtO2C
CO2Et
N
B
N
F
F

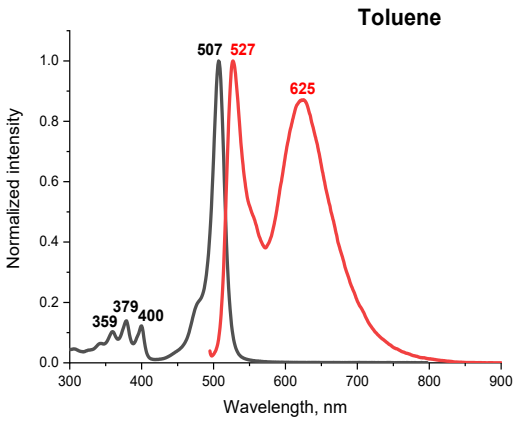
Toluene
507
527
625
379
359
400
Normalized intensity
Wavelength, nm

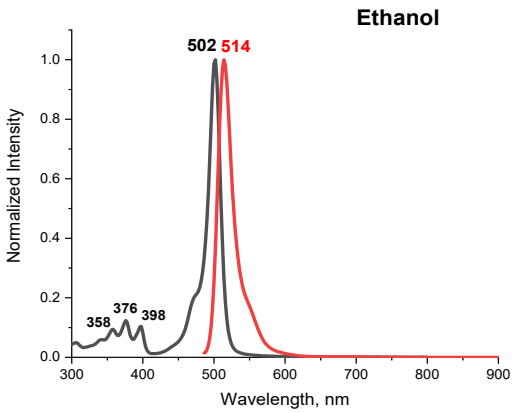
Ethanol
502
514
376
358
398
Normalized Intensity
Wavelength, nm

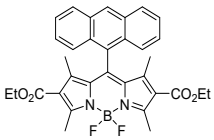
EtO2C
CO2Et
N
B
N
F
F

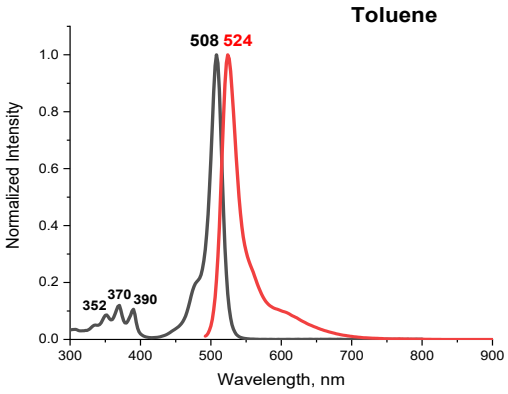
Toluene
508
524
370
352
390
Normalized Intensity
Wavelength, nm

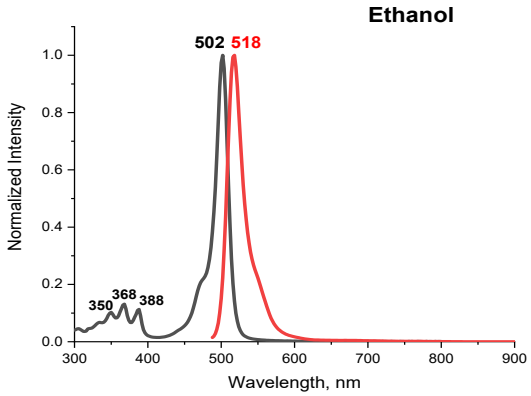
Ethanol
502
518
368
350
388
Normalized Intensity
Wavelength, nm

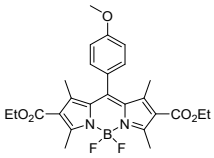
O
EtO2C
CO2Et
N
B
N
F
F

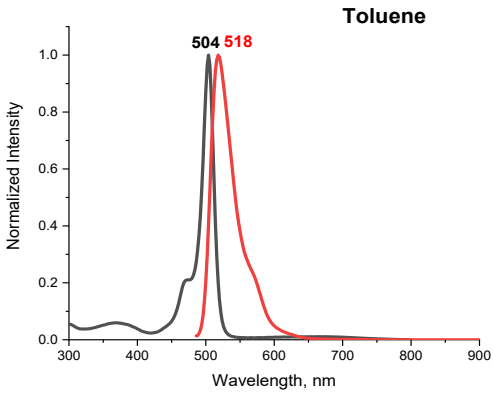
Toluene
504
518
Normalized Intensity
Wavelength, nm

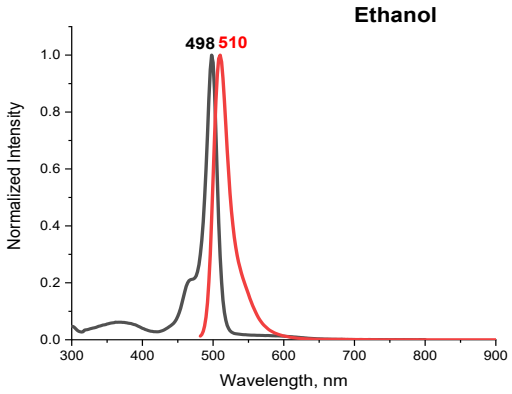
Ethanol
498
510
Normalized Intensity
Wavelength, nm

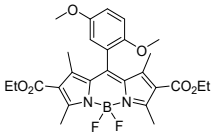
O
O
EtO2C
CO2Et
N
B
N
F
F

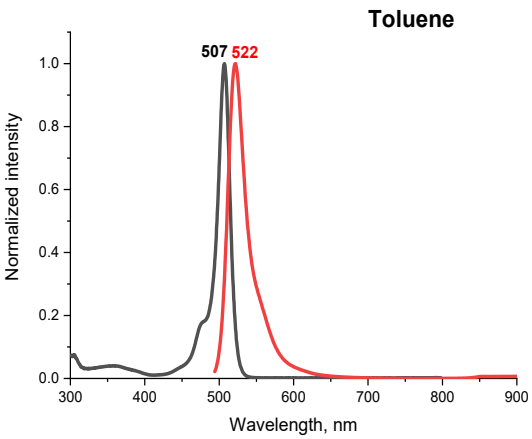
Toluene
507
522
Normalized intensity
Wavelength, nm

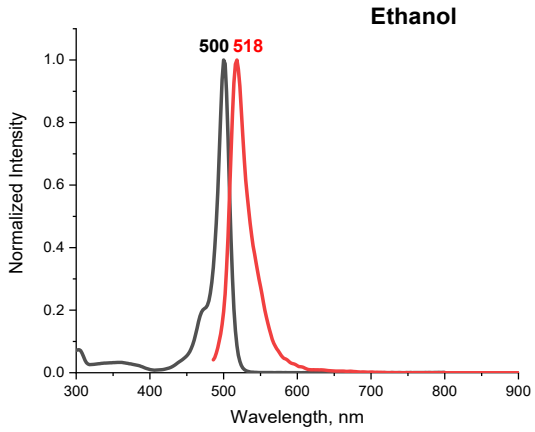
Ethanol
500
518
Normalized Intensity
Wavelength, nm

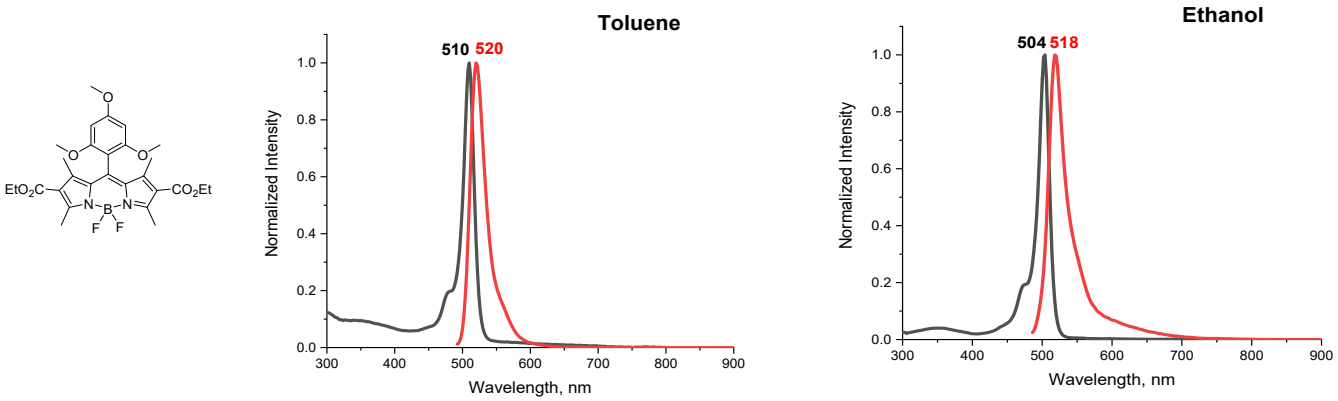

Figure S10. Normalized absorption (black line) and photoluminescence emission (red line) spectra of dyads in toluene and ethanol. Excitation wavelength: 470 nm.

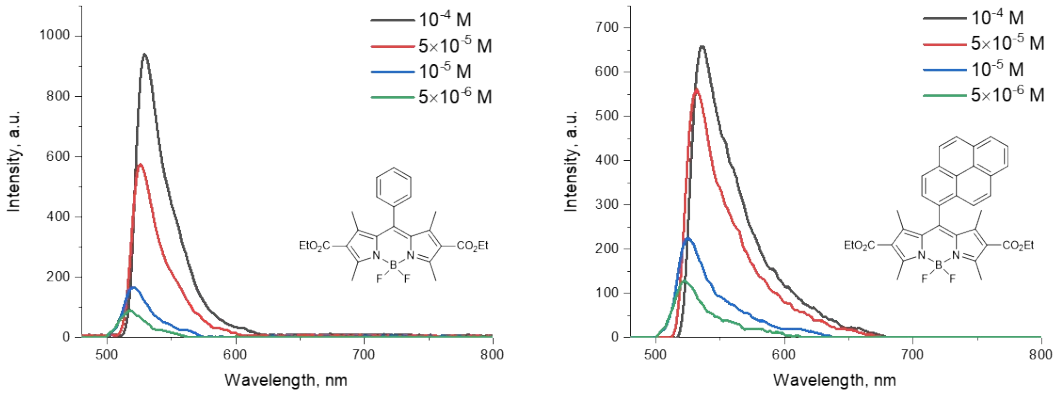

Figure S11. Photoluminescence emission spectra of **BDP 1a** and **BDP 1b** recorded at different concentrations in toluene (λ_{exc} = 470 nm).

6. Singlet oxygen generation quantum yields measurements

The singlet oxygen quantum yield measurements were performed according to previously described method.[3] Solutions of the $^1O_2$ trap, 1,9-dimethylanthracene (DMA), with an optical density of around 1.4 in air-saturated solvent were employed. Corresponding BODIPY was added to the cuvette, and its absorbance was adjusted to 0.2-0.9 at the wavelength of irradiation (514 nm). The solutions in the cuvette were irradiated with 514 nm laser at a constant power density of 10 mW cm^{-2}. The absorption spectra of the solutions were measured every 30-120 s. The slope of plots of absorbance of DMA at 376 nm vs. irradiation time for each photosensitizer was calculated.

Singlet oxygen quantum yields were calculated based on the equation:

$$\Phi_\Delta = \Phi_\Delta^{ref} \times \frac{k}{k_{ref}} \times \frac{I_{abs}^{ref}}{I_{abs}} \qquad \text{(S1)}$$

where Φ_Δ is the singlet oxygen quantum yield; the superscript *ref* stands for 2,6-diiodo-8-phenyl-1,3,5,7-tetramethylBODIPY (Figure S22b, Φ_Δ = 0.85 in toluene)[4]; *k* is the slope of the curves of DMA absorption (376 nm) vs. irradiation time; I_{abs} represents the absorption correction factor which is given by $I = 1–10^{-OD}$ (OD is the optical density at 514 nm).

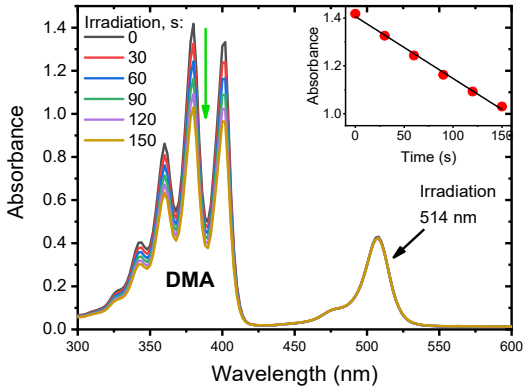

Figure S12. a) Photooxidation of 1,9-dimethylanthracene in air-saturated THF solution containing **1d**. Inset: dependence of the absorbance at 376 nm on the irradiation time. b) Reference photosensitizer **BPDI$_2$**.

Table S1. Singlet oxygen quantum yields of reference BODIPY dyads in different solvents.

Compound	Φ_Δ				
	ACN	EtOH	THF	toluene	cyclohexane
	**0.767**	**0.667**	**0.465**	**0.067**	**0.059**
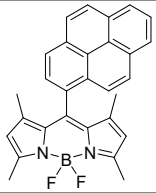	**0.56**	**0.349**	**0.101**	**0.088**	**0.07**

7. Time-resolved emission spectroscopy

Time-correlated single photon counting (TCSPC) measurements were performed in a modified microscope (Olympus IX71).[5] The excitation source is 447 nm picosecond pulsed laser (70 ps, 100 kHz to 100 MHz variable repetition rate, DeltaDiode, HORIBA) that is passed through a 50 µm pinhole to clean the laser output mode. The beam is directed to the back-illumination port of the microscope and focused into the sample with a 10 × 0.4 N.A. air microscope objective (Olympus).[6] The solution in 1 mm cuvette is mounted horizontally on the Physik Instrumente (PI) scanning stage. Laser excitation intensity is controlled with a set of neutral density filters (ThorLabs). The emitted light was filtered with a longpass filter 470 nm to eliminate scattered laser light and appropriate bandpass filters to select emission wavelength. The filtered signal was recollimated and sent into two avalanche photodiodes (APDs, PDM series, Micro Photon Devices) placed in a Hanbury–Brown–Twiss arrangement with a 50/50 beam splitter. Time-tagged TCSPC data was collected using HydraHarp 400 controller (PicoQuant). All the lifetime fittings were performed at posteriori in Origin 2021.

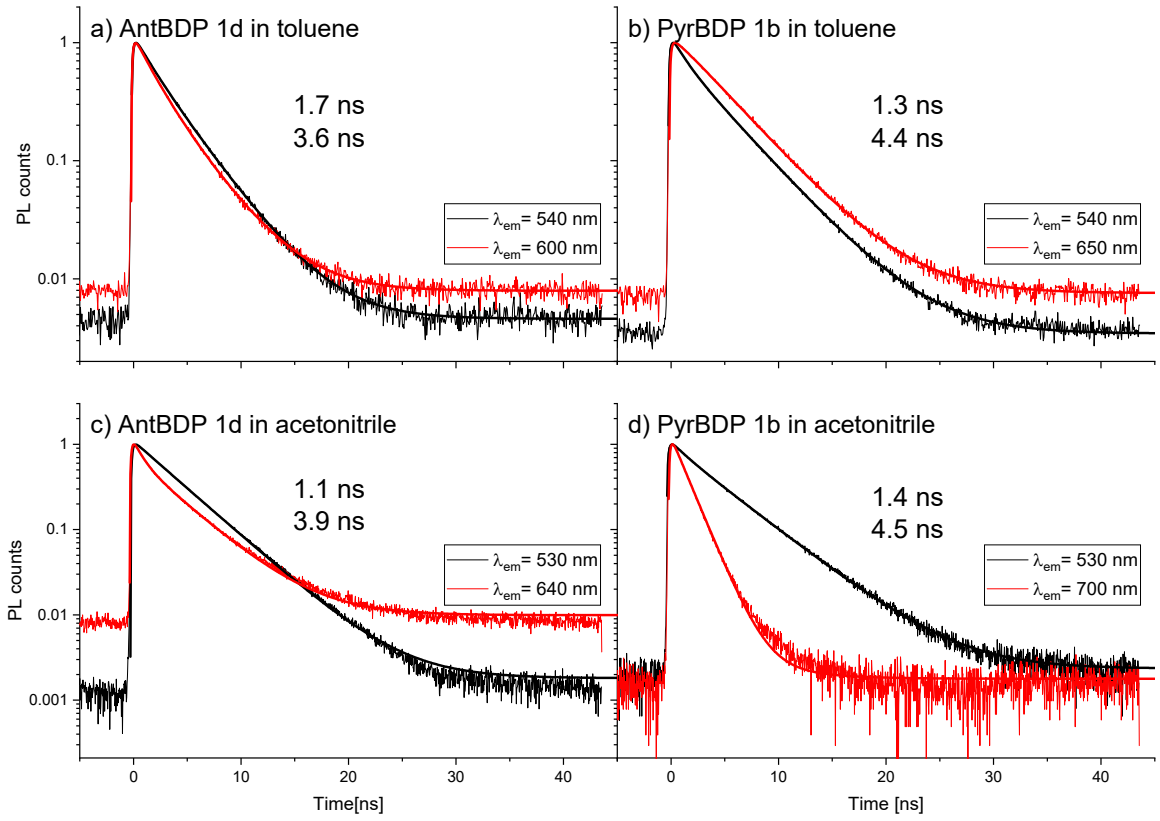

Figure S13. Time-resolved photoluminescence decays (λ_{exc}= 447 nm) and fits in a) **AntBDP 1d** (26 µM) and b) **PyrBDP 1b** (28 µM) in toluene, and c) and d) in acetonitrile, respectively. Global exponential tail fit (i.e. fixed lifetimes for the different emission wavelengths).

8. Transient absorption spectroscopy

Transient absorption (TA) spectroscopy was carried out using a home-built pump-probe setup.[7] Two different configurations of the setup were used for either short delay, namely 100 fs to 8 ns experiments, or long delay, namely 1 ns to 300 μs delays, as described below:

The output of a Ti:sapphire amplifier (Coherent LEGEND DUO, 800 nm, 4.5 mJ, 3 kHz, 100 fs) was split into three beams (2 mJ, 1 mJ, and 1.5 mJ). Two of them were used to separately pump two optical parametric amplifiers (OPA; Light Conversion TOPAS Prime). The 2 mJ TOPAS generates wavelength-tunable pump pulses (240-2600 nm, using Light Conversion NIRUVIS extension), while the 1 mJ TOPAS generates signal and idler only (1160-2600 nm). The pump wavelength was fixed at 505 nm. A fraction of the 1.5 mJ output of the Ti:sapphire amplifier was focused into a c-cut 3 mm thick sapphire window, thereby generating a white light supercontinuum from 500 to 1600 nm. The pump-probe delay time was achieved by varying the pump path length using a broadband retroreflector mounted on a 600 mm automated mechanical delay stage (Newport linear stage IMS600CCHA controlled by a Newport XPS motion controller), generating delays from -400 ps to 8 ns.

For the 1 ns to 300 μs delay (long delay) TA measurement, the same probe white-light supercontinuum as for the 100 fs to 8 ns delays was used. The excitation light (pump pulse) was provided by an actively Q-switched Nd:YVO_4 laser (InnoLas picolo AOT) frequency-doubled (tripled) to provide pulses at 532 nm, and triggered by an electronic delay generator (Stanford Research Systems DG535), itself triggered by the TTL sync from the Legend DUO, allowing control of the delay between pump and probe with a jitter of roughly 100 ps.

Pump and probe beams were focused on the sample to spot sizes measured (from a Gaussian fit at 86.5% intensity) using a beam profiler (Coherent LaserCam-HR II). The samples were prepared in a nitrogen filled glovebox and sealed in cuvettes, and pump and probe beams were incident on the sample. The transmitted fraction of the white light was guided to a custom-made prism spectrograph (Entwicklungsbüro Stresing) where it was dispersed by a prism onto a 512-pixel CMOS linear image sensor (Hamamatsu G11608-512A). The probe pulse repetition rate was 3kHz, while the excitation pulses were mechanically chopped to 1.5 kHz, while the detector array was read out at 3 kHz. Adjacent diode readings corresponding to the transmission of the sample after excitation and in the absence of an excitation pulse were used to calculate $\Delta T/T$. Measurements were averaged over several thousand shots to obtain a good signal-to-noise ratio. The chirp induced by the transmissive optics was corrected with a home-built Matlab code.

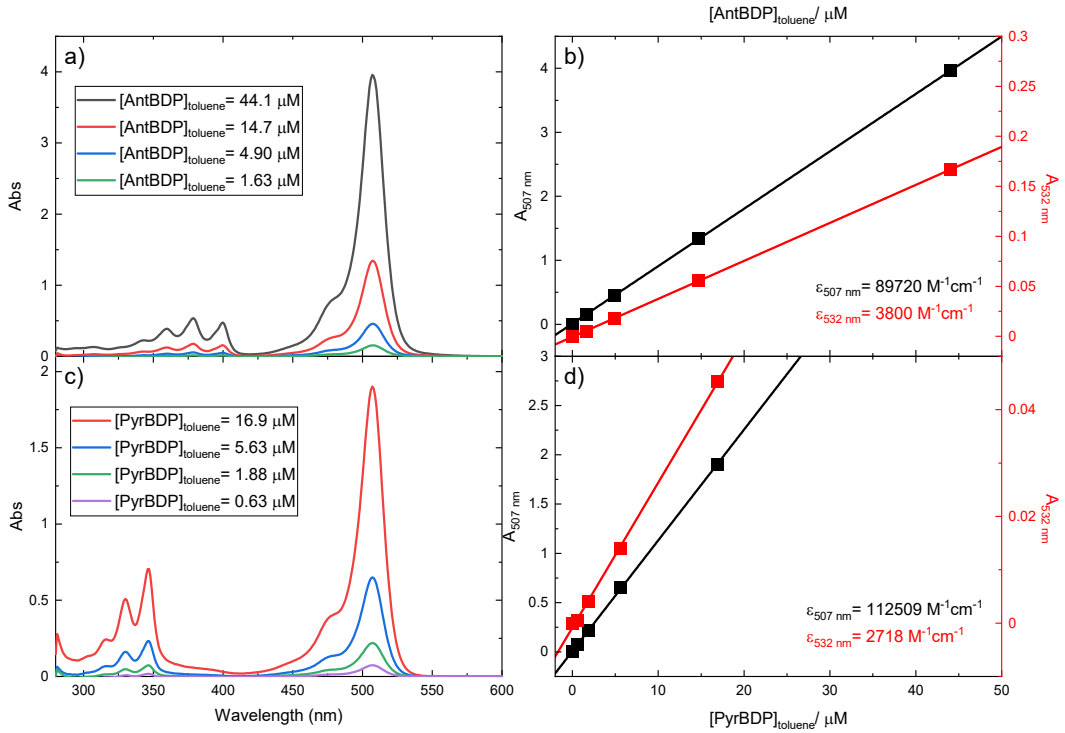

Figure S14. a), c) Absorption spectra and b), d) absorbance at 532 nm ($A_{532\ nm}$) and maxima at 507 nm ($A_{507\ nm}$) vs concentration for **AntBDP 1d** and **PyrBDP 1b** in toluene, respectively. ε_S was determined to calculate ε_S and then ϕ_T by relative actinometry.

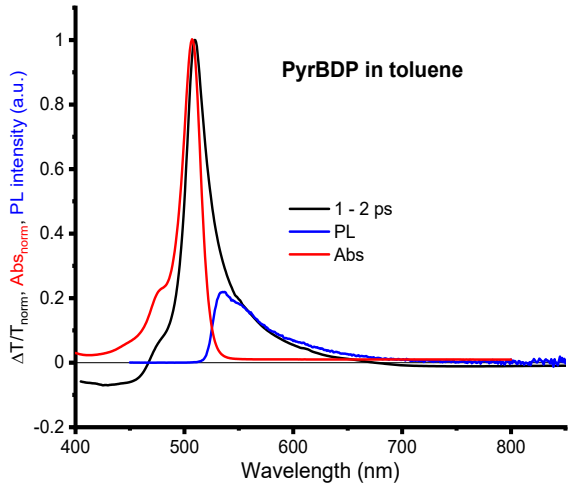

Figure S15. Absorption, photoluminescence (λ_{exc}= 447 nm) emission and transient absorption (TA - 505 nm, 1 – 2 ps) spectra, identifying the region of stimulated emission in the TA spectra in **PyrBDP 1b** in toluene.

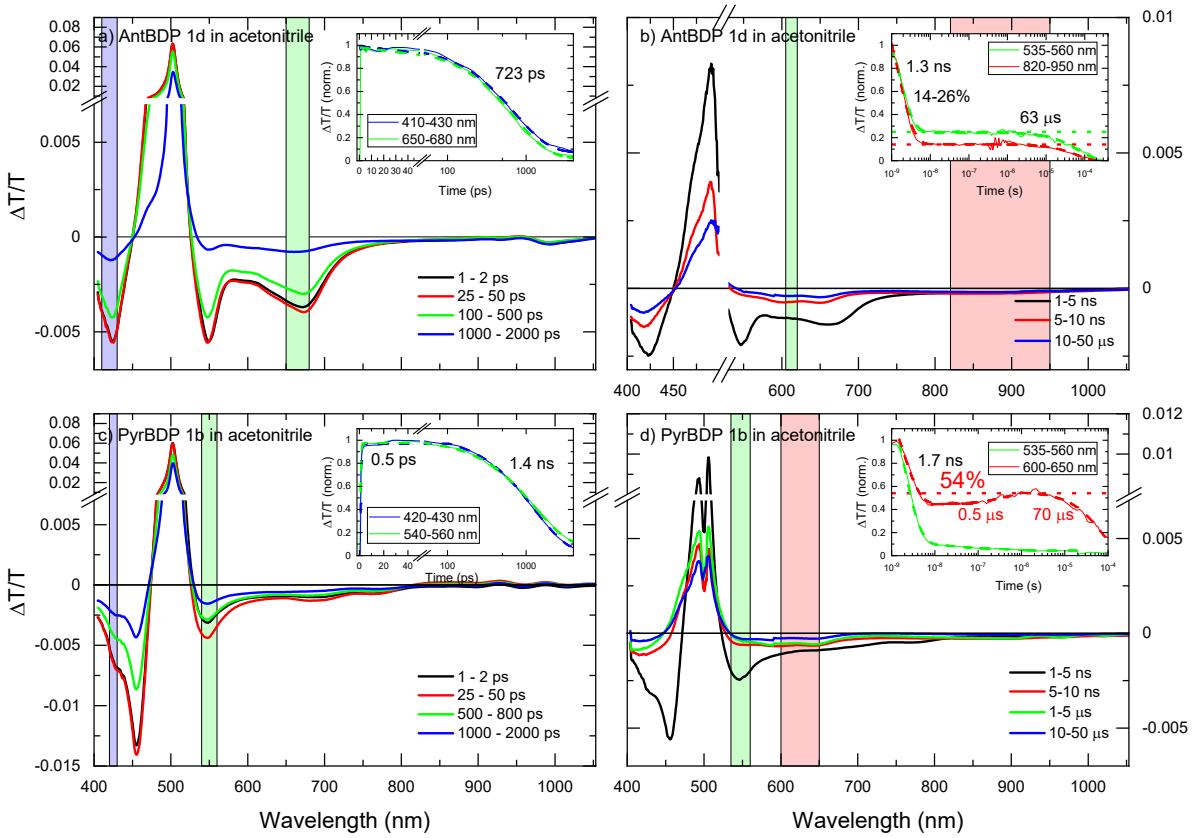

Figure S16. ps–ns (a and c) and ns–µs (b and d) TA spectra with kinetics (inset) of selected spectral region of **PyrBDP 1c** and **AntBDP 1d** in acetonitrile after excitation with 505 nm and 532 nm laser pulses, respectively, under inert atmosphere.

Table S2. Photophysical properties of dyads **PyrBDP 1b** and **AntBDP 1c** in acetonitrile and toluene (and Rose Bengal in methanol for reference). Singlet and triplet extinction (ε_S and ε_T, respectively) coefficients, photoluminescence excitons lifetime (τ_{PL}), triplet decay time (τ_T), triplet quantum yield (ϕ_T).

Material / Solvent	**Singlet decay/ CT generation**	**CT S decay/ triplet generation**	**τ_{PL} ($\lambda_{exc=}$ 447 nm)**		**τ_T**	**$\varepsilon_{S,532\ nm}$***	**ε_T (Singlet Depletion Method)**	**φ_T (TA)**	**φ_T (Relative actinometry TA)[8]**
	ps	**ns**			**µs**	**$M^{-1}\ cm^{-1}$**		**%**	
AntBDP 1d toluene	3.7/11.3	0.5-2.4	**1.7**	3.6	26.5	3800	580		57-75
AntBDP 1d acetonitrile		0.7-1.3	**1.1**	3.9	63			14-26	
PyrBDP 1b toluene	4.6/10	**3.7-5.7**	1.3	**4.4**	0.7-1.2	2718	636	58	56-73
PyrBDP 1b acetonitrile	0.5	1.3-1.7/500	1.4	4.5	70			54	
Rose Bengal methanol						104700 (558 nm)[9]	7984 ± 885 6270 ± 300[10]	76-90[11]	

* See Figure S14

9. Photopolymerizable materials preparation and characterization

9.1. Synthesis of polymeric materials

All chemicals used for the synthesis were purchased from Merck. Synthesis was performed following a previously published procedure.[12] Cellulose acetate (8 g, ≈ 30'000 M_n) was dissolved in acetone (125 ml) and heated at 80°C for 4 h. Polyethylene glycol (2.00 g, ≈ 1'000 M_n) was added and the solution was heated at 80°C for another 4 h. The mixture was allowed to cool overnight and then acrylamide (0.84 g, 11.8 mmol) and N,N-methylenebisacrylamide (0.20 g, 1.3 mmol) were added. This was stirred at r.t. for 1 h until the monomers had dissolved. N-phenylglycine (0.082 g, 0.54 mmol) was added and the solution was stirred at r.t. until fully dissolved. The mixture was separated into five 25 ml portions; one control and four to which BODIPYs (**BDP 1a, PyrBDP 1b, AntBPD 1d,** and **I_2BDP**) were added. Corresponding BODIPY (0.0025 mmol) was added to each mixture and stirred at r.t. until dissolved.

1 mL portions of the photopolymer solution were spread evenly across a glass substrate, and dried at room temperature under a glass dish to slow down solvent evaporation. This was repeated four times to achieve layers between 75-105 μm in thickness.

9.2 UV-Vis absorption spectra

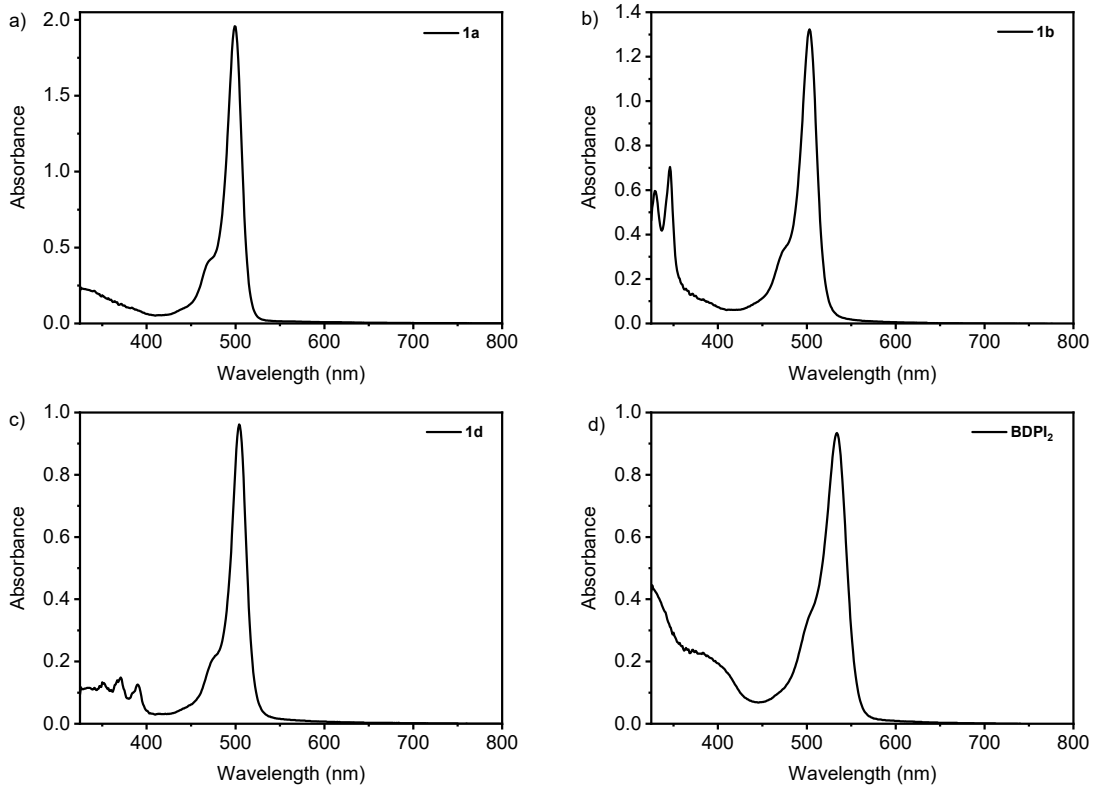

Figure S17. UV-Vis absorption spectra for photopolymer layers containing a) **BDP 1a,** b) **PyrBDP 1b,** c) **AntBDP 1d,** and d) reference photosensitizer **$BDPI_2$**.

9.3 Photopolymerization tests – Raman spectra

Raman spectroscopy was performed using a Horiba Jobin Yvon LabRAM HR800 spectrometer. The instrument has options of 532nm or 785 nm as source. The spectra were recorded at 785 nm, as the photopolymer samples have negligible absorbance at this wavelength. A 300 lines/mm grating and a 100× objective were used. To initiate polymerization, the samples were exposed to 532 nm light with

an intensity of 10 mW, using the same pathway as the Raman source laser. Samples were exposed for a total of 40s, with spectra being recorded at set intervals. Each measurement was repeated in duplicate. Layers were prepared as described in section 8.1, on an aluminium substrate instead of glass. This was to avoid glass fluorescence signals in the spectra.[13] Spectra were processed and analysed using Horiba Labspec6 software. After removing a polynomial baseline, signals at ≈ 1600 and ≈ 1623 cm^{-1} were fitted using a Guassian-Lorentzian function, and the ratio of the area of these signals was plotted vs 532 nm irradiation time to compare the polymerization rates.

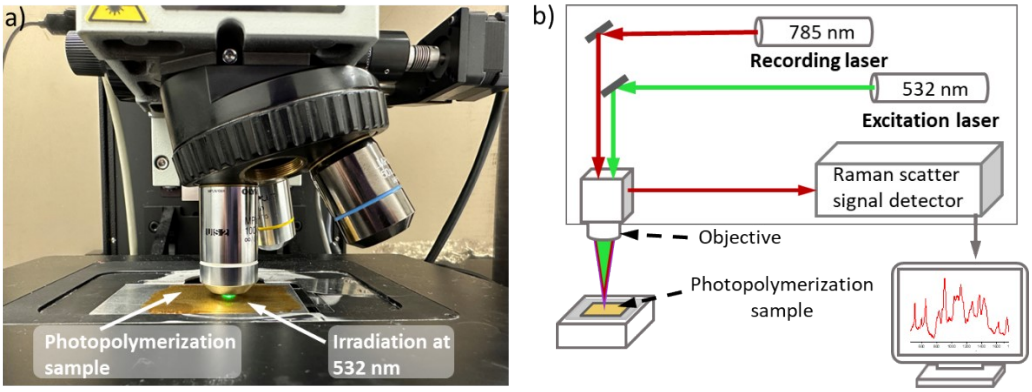

Figure S18. a) Photograph illustrating photopolymerization test under excitation with 532 nm laser. b) Schematic representation of Raman setup used to measure photopolymerization rates.

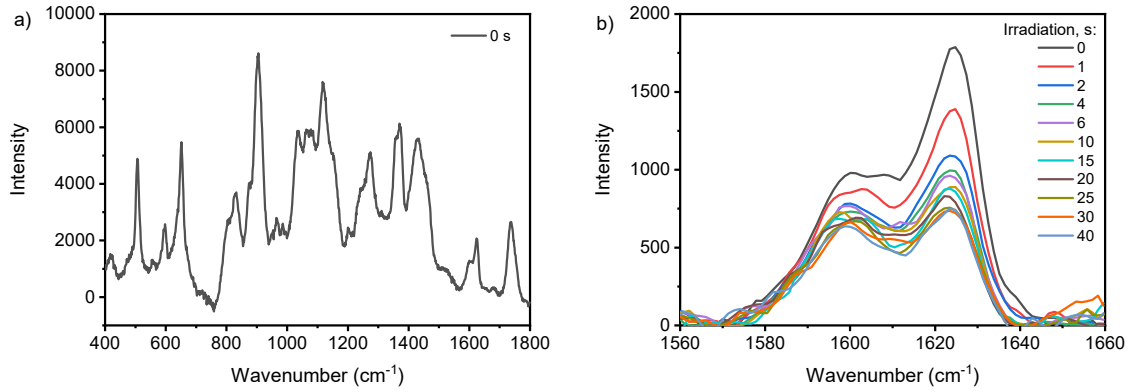

Figure S19. a) Full Raman spectrum of **AntBDP 1d** before irradiation and b) change in intensity of signals at 1600 cm^{-1} and 1623 cm^{-1} over time for **AntBDP 1d**.

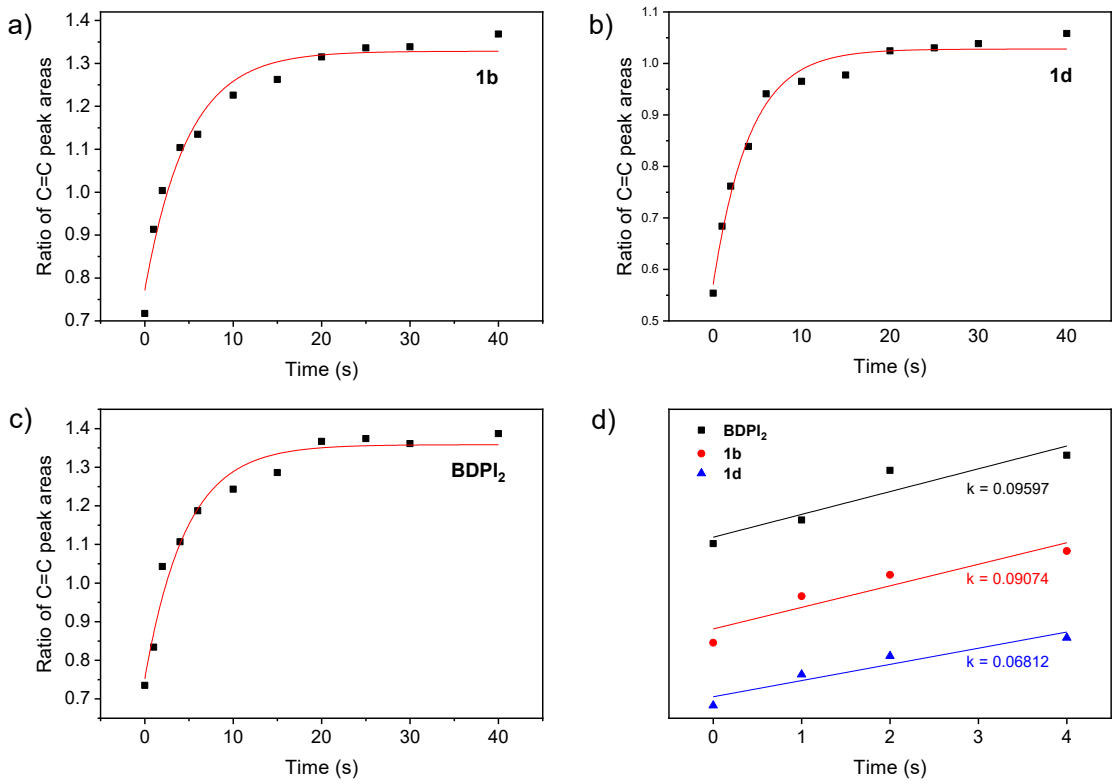

Figure S20. Increase in ratio between peaks at ≈1600 and ≈ 1623 cm^{-1}, corresponding to the C=C double bonds of acrylamide and methylenebisacrylamide, respectively, for a) **PyrBDP 1b**; b) **AntBDP 1d**; and c) reference photosensitizer **$BDPI_2$**. Samples were exposed to 532 nm light source (10 mW/cm^2). The red solid line is a mono-exponential fitting curve. d) Linear fitting of C=C peak areas ratio change vs time for **PyrBDP 1b, AntBDP 1d,** and **$BDPI_2$** (t = 0 – 4 s).

10. Holographic structures recording

10.1 Holographic recording and diffraction efficiency measurement

The holographic recording of volume phase transmission gratings was carried out using the set-up presented in Figure S21. Unslanted gratings with a spatial frequency of 800 lines/ mm were recorded in layers with thickness of 75-105 μm using the optimum total recording intensity of 20 mW/cm^2. During holographic patterning, the photosensitive layers were exposed to two beams of 532 nm wavelength obtained by splitting a Nd:YVO_4 laser beam. The angle of incidence of the recording beams (θ) was 12.3° with respect to the normal to the surface of the sample.
The dynamic of the grating formation was monitored by recording the real-time diffraction efficiency growth curve during holographic patterning. A low intensity (1.8 mW/cm^2) 633 nm beam from a He-Ne laser was employed as a probe beam for both real-time diffraction efficiency and Bragg selectivity curve measurements (Figure S21). The laser beam intensity was monitored using an optical power meter (Newport, model 843-R) and the acquired data were transferred to a computer. The diffraction efficiency (η) of the transmission gratings was calculated as the ratio of the first-order diffracted beam intensity (I_1) and incident beam intensity (I_{in})

$$\eta = \frac{I_1}{I_{in}} \times 100\% \,. \tag{S2}$$

To measure the Bragg selectivity curves, the sample was mounted on a rotation stage, which was computer controlled *via* a motion controller (Newport ESP300). Experimental Bragg selectivity curves were used to estimate the layer thickness (d) utilising the following coupled-wave theory equation[14]

$$\Delta\theta_{FWHM} = \frac{0.87\,\Lambda}{d}\,, \tag{S3}$$

where $\Delta\theta_{FWHM}$ is the full angular bandwidths at the half of the maximum of the diffraction efficiency, Λ – spatial period.

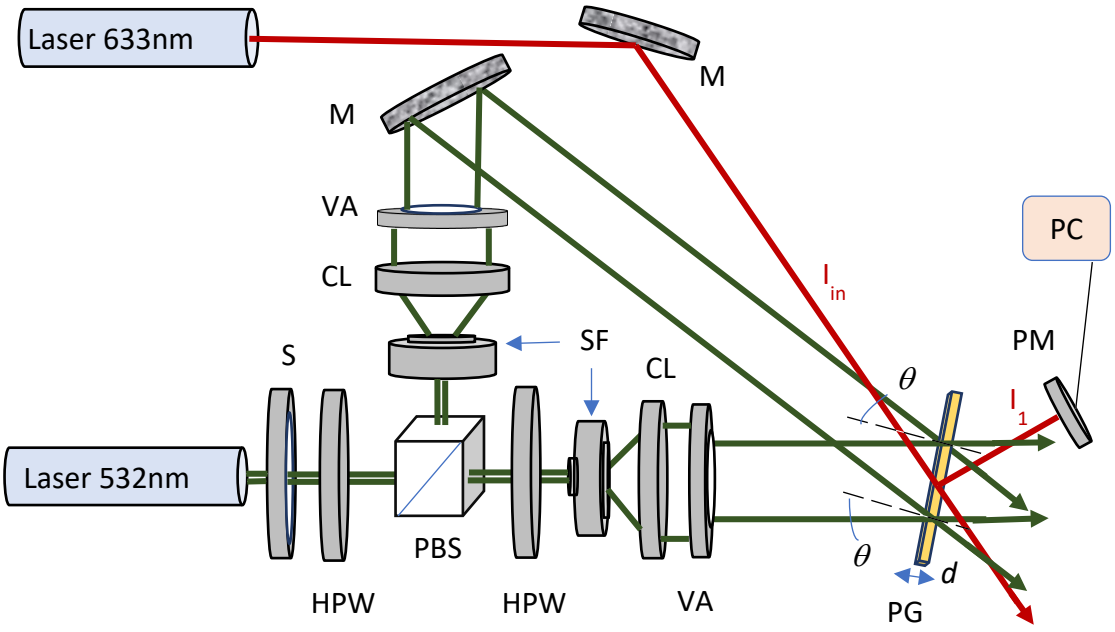

Figure S21. Schematic representation of the experimental set up for the holographic recording of transmission gratings with the spatial frequency of about 800 lines/mm. S – electronic shutter, HWP

- half-wave plate, PBS - polarising beam splitter, SF – spatial filter, CL – collimator, VA - variable aperture, PG – photosensitive layer, M – mirror, PM - power meter, PC – computer.

10.2 Coupled-wave theory analysis for volume holographic gratings

A holographic grating can be classified as a volume grating, if the thickness (d) of the recorded hologram is substantial in comparison with its spatial period (Λ). This classification can be quantified by the Klein-Cook Q-parameter, where a volume grating has a Q-parameter value higher than ten[15]

$$Q = \frac{2\pi\lambda d}{n\Lambda^2}, \tag{S4}$$

where λ is a wavelength of the recording light, n is the average refractive index of the medium. Quantitative analysis of volume phase gratings is carried out using the Kogelnik's Coupled-Wave theory.[8] According to the coupled-wave theory, refractive index modulation (Δn) achieved during holographic recording in transmission mode can be determined using the following equation

$$\Delta n = \frac{\lambda cos\theta sin^{-1}\left(\sqrt{\eta}\right)}{\pi d}, \tag{S5}$$

where λ is the wavelength of the reconstructing beam, θ is the Bragg angle inside the medium for the reconstructing wavelength and η is the diffraction efficiency.
In accordance with the coupled wave theory, the diffraction efficiency of a volume phase transmission grating is determined by

$$\eta = \frac{\sin^2\sqrt{\left(\xi^2 + \nu^2\right)}}{1 + {\xi^2}/{\nu^2}}. \tag{S6}$$

The parameter ν defines the maximum diffraction efficiency at Bragg incidence, whereas the parameter ξ describes deviation from the Bragg condition due to the angular and wavelength deviations. At Bragg incidence $\xi = 0$ and the maximum diffraction efficiency is determined

$$\eta = \sin^2\nu. \tag{S7}$$

The parameter ν can be written as

$$\nu = \frac{\pi\,\Delta n\,d}{\lambda\cos\theta}, \tag{S8}$$

where λ is the wavelength of the reconstructing beam. At non-Bragg incidence, the parameter ξ is described

$$\xi = \Delta\theta\frac{kd}{2}, \tag{S9}$$

where $\Delta\theta$ is the deviation from Bragg angle, k is the wave vector of the grating and its magnitude is determined as $2\pi/\Lambda$.

10.3 Calculation of the photosensitivity of holographic recoding materials

Photosensitivity (S) of the holographic recording material is defined as the ratio between the square root of the diffraction efficiency and the product of the exposure energy (E) and the visibility (V)[16]

$$\sqrt{\eta} = SEV, \tag{S10}$$

where visibility is defined by the ratio of the recording beam intensities (R)

$$V = \frac{2R^{-1/2}}{(1+R)}. \tag{S11}$$

In the current experimental conditions, the holographic recording is performed using two beams with equal intensity which provides $R = 1$. Thus, calculation of S is carried out by plotting $\sqrt{\eta}$ versus E obtained as the product of the total recording intensity and recording time (Figure S22). The slope of the linear fit corresponds to E (cm^2/J).

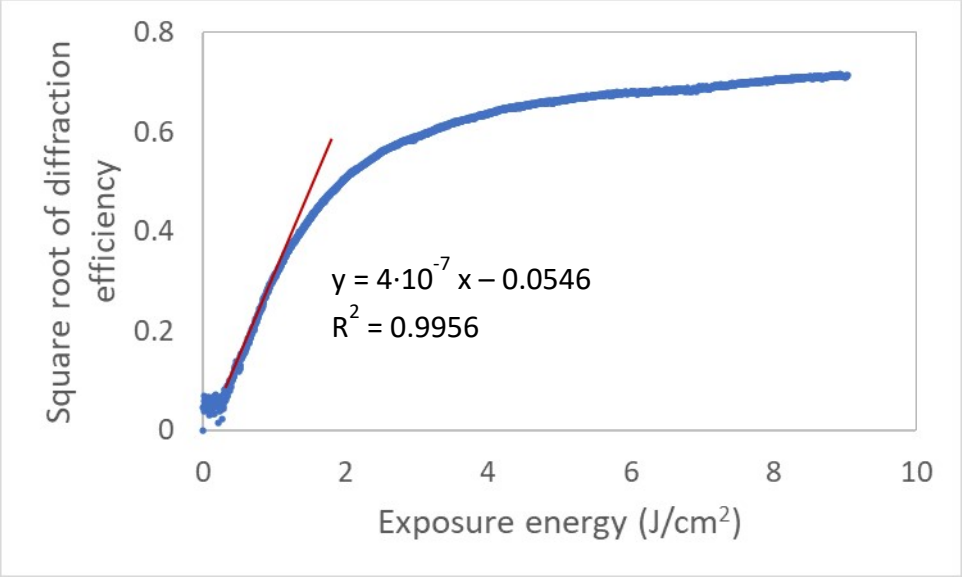

Figure S22. Square root of the diffraction efficiency growth curve of the CA-PEG containing **PyrBDP 1b** as a sensitizer. The slope of the linear fit (marked in red) corresponds to the exposure sensitivity which is equal to 4×10^{-4} mJ/cm^2.

10.4 Shelf-life study of the transmission gratings

The shelf-life study of the transmission gratings recorded in the CA-PEG layers containing **PyrBDP 1b** and **AntBDP 1d** as a sensitizer was carried out by monitoring the diffraction efficiency within 4 months. Figure S23 represents the Bragg selectivity curves of the CA-PEG containing **PyrBDP 1b** (Figure S23a) and **AntBDP 1d** (Figure S23b) measured in 1 day and in 4 months after recording. As seen, no decrease in the diffraction efficiency was detected. Slightly higher diffraction efficiency measured in 4 months (Figure S23a) might be caused by some fluctuation in laser intensity during the measurement. Further shelf-life study is in progress.

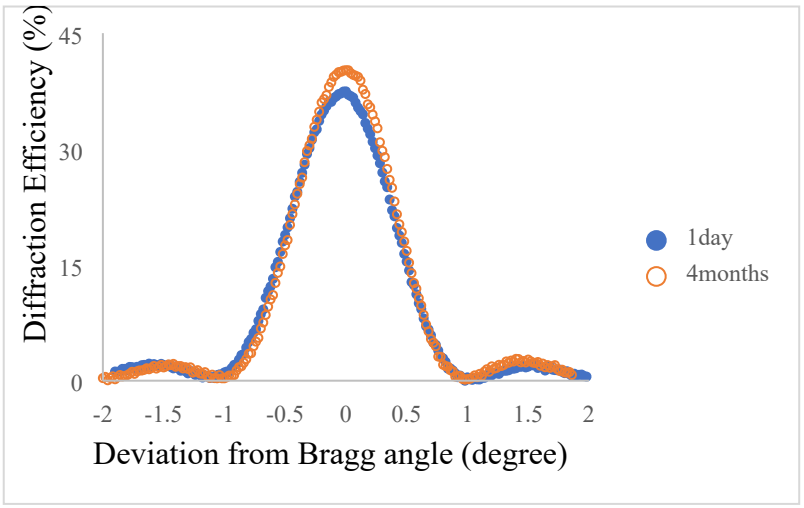

a)

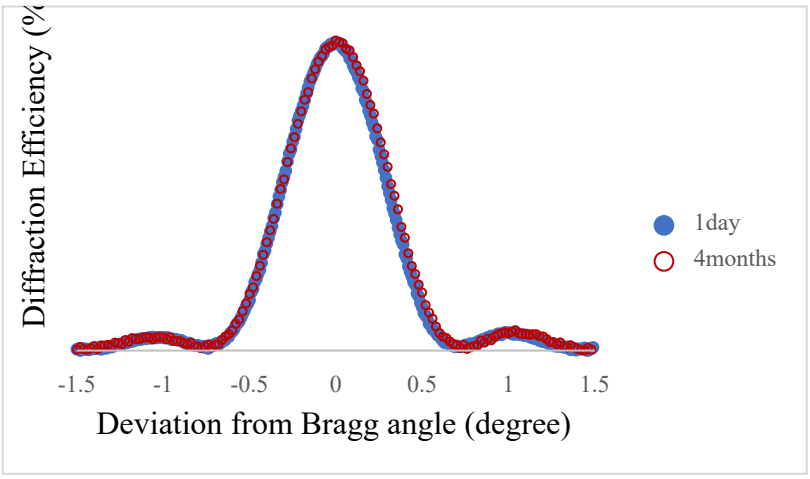

b)

Figure S23. Bragg selectivity curves of the CA-PEG containing **PyrBDP 1b** (a) and **AntBDP 1c** (b) as a sensitizer measured in 1 day and in 4 months after recording.

11. References

[1] J.R. Lakowicz, Principles of Fluorescence Spectroscopy, 2nd Ed., Kluwer Academic/Plenum Publishers, New York, London, Moscow, Dordrecht, 1999.
[2] G. A. Cordell, *J. Org. Chem.*, **1975**, *40*, 3161.
[3] L. Gou, C. N. Coretsopoulos and A. B. Scranton, *J. Polym. Sci. Part A Polym. Chem.*, **2004**, *42*, 1285.
[4] A.A. Buglak, A. Charisiadis, A. Sheehan, C.J. Kingsbury, M.O. Senge, M.A. Filatov, *Chem. Eur. J.*, **2021**, *27*, 9934.
[5] L. Gutiérrez-Arzaluz, G.H. Ahmed, H. Yang, S. Shikin, O.M. Bakr, A.V. Malko, O.F. Mohammed, *J. Phys. Chem. A*, 2020, **124**, 4855.
[6] L. Gutiérrez-Arzaluz, G.H. Ahmed, H. Yang, S. Shikin, O.M. Bakr, A.V. Malko, O.F. Mohammed, *J. Phys. Chem. A*, **2020**, *124*, 4855.
[7] (a) V. Druet, D. Ohayon, C.E. Petoukhoff, Y. Zhong, N. Alshehri, A. Koklu, P. D. Nayak, L. Salvigni, L. Almulla, J. Surgailis, S. Griggs, I. McCulloch, F. Laquai, S. Inal, 2023, arXiv:2305.06810; (b) T. Mikulchyk, S. Karuthedath, C.S.P. De Castro, A.A. Buglak, A. Sheehan, A. Wieder, F. Laquai, I. Naydenova, M.A. Filatov, *J. Mater. Chem. C.*, 2022, **10**, 11588–11597.
[8] I. Carmichael and G. L. Hug, *J. Phys. Chem. Ref. Data*, 1986, **15**, 1–250.
[9] J. J. M. Lamberts, D. R. Schumacher, D. C. Neckers, *J. Am. Chem. Soc.*, 1984, **106**, 5879–5883.
[10] P. Murasecco-Suardi, E. Gassmann, A.M. Braun, E. Oliveros, *Helv. Chim. Acta*, 1987, **70**, 1760–1773.
[11] L. Ludvíková, P. Friš, D. Heger, P. Šebej, J. Wirza, P. Klán, *Phys. Chem. Chem. Phys.*, 2016, **18**, 16266-16273.
[12] Sabad-E-gul, J. Cassidy and I. Naydenova, *Photonics*, 2021, **8**, 329.
[13] (a) L.M. Fullwood, D. Griffiths, K. Ashton, T. Dawson, R.W. Lea, C. Davis, F. Bonnier, H.J. Byrne, Matthew, J. Baker, *Analyst*, 2014, **139**, 446; (b) L.T. Kerr, H.J. Byrne, B.M. Hennelly, *Anal. Methods*, 2015, **7**, 5041.
[14] H. Kogelnik, *Bell Syst. Tech. J*, **1969**, *48*, 2909.
[15] P. Phariseau, in *Proc. Indian Acad. Sci. - Sect. A*, **1956**, 44.
[16] P. Hariharan, Optical Holography: Principles, Techniques and Applications Cambridge U. Press, Cambridge, UK, 1984